AN ABSTRACT OF THE THESIS OF

Rebecca Paustian for the degree of Master of Science in Environmental Engineering presented on June 15, 2018.

Title: Analyzing the Relationship between Capillary Pressure, Saturation, and Interfacial Area for a Three-Phase Flow System in Porous Media

Abstract approved:

_____

Dorthe Wildenschild

Multi-phase flow in porous media includes many instances of subsurface flow. Three-phase flow in particular is important in situations of enhanced oil recovery, CO2 sequestration, and groundwater remediation. Many studies have been performed on how two fluid phases (oil/water or air/water) behave in porous media, but very few studies exist on three-phase flow systems (e.g. oil/water/air). This work presents data collected via x-ray micro-tomography resulting in high-resolution three-dimensional images of the fluid configurations for varying degrees of saturation. The relationship of capillary pressure (P_c), saturation (S_w), and fluid-fluid interfacial area (a_{nw}) was found to eliminate hysteresis for the oil-water fluid pair in the water-wet system, but due to insufficient data, this could not be confirmed for the air-oil fluid pair in the water-wet system nor either fluid pair in the fractionally-wet system. Additionally, for the oil-water fluid pair the wettability of the medium had a pronounced effect on the capillary pressure-saturation-interfacial area relationship, however wettability did not alter the capillary pressure-saturation-interfacial area relationship for the air-oil fluid pair.

Analyzing the Relationship between Capillary Pressure, Saturation, and Interfacial Area for a Three-Phase Flow System in Porous Media

by
Rebecca Paustian

A THESIS

submitted to

Oregon State University

in partial fulfillment of
the requirements for the
degree of

Master of Science

Presented June 15, 2018
Commencement June 2019

Master of Science thesis of Rebecca Paustian presented on June 15, 2018.

APPROVED:

Major Professor, representing Environmental Engineering

Head of the School of Chemical, Biological, and Environmental Engineering

Dean of the Graduate School

I understand that my thesis will become part of the permanent collection of Oregon State University libraries. My signature below authorizes release of my thesis to any reader upon request.

Rebecca Paustian, Author

ACKNOWLEDGEMENTS

The author expresses sincere appreciation to Dorthe Wildenschild, for her guidance and expertise; Doug Meisenheimer, for answering the never-ending list of questions; and my family and friends, for their support.

TABLE OF CONTENTS

Page

TABLE OF CONTENTS (continued)

Page

TABLE OF CONTENTS (continued)

Page

LIST OF FIGURES

Figure Page

LIST OF FIGURES (Continued)

LIST OF FIGURES (Continued)

LIST OF FIGURES (Continued)

LIST OF TABLES

LIST OF APPENDIX TABLES

1 Introduction

Multi-phase flow in porous media includes many instances of subsurface flow. Multi-phase flow studies, particularly three-phase flow will influence fields including petroleum engineering, environmental engineering, and hydrology. A three-phase system can occur when a non-aqueous phase liquid (NAPL) leaks, potentially from a storage tank into an unsaturated zone of the subsurface, during geologic carbon sequestration, when CO_2 is injected into a depleted oil reservoir and trapped, or enhanced oil recovery via water flooding. Sophisticated models of the interactions of fluids and the porous medium would be required for accurate prediction of fluid configurations and potential movement.

Flow in a porous medium is often modeled with Darcy's law, Equation 1.

$$Q = \frac{-\kappa A}{\mu}\left[\frac{\partial P}{\partial l} + \rho g \frac{\partial z}{\partial l}\right] \qquad \text{Equation 1}$$

Where Q is flowrate, κ is permeability, A is cross sectional area of the medium, μ is viscosity, ρ is the density of the fluid, g is acceleration due to gravity, $\frac{\partial P}{\partial l}$ represents change in pressure per length of formation, and $\frac{\partial z}{\partial l}$ represents the change in elevation. Darcy's law is defined for one-dimensional flow of a single fluid phase in a homogeneous porous medium. As the flow problem becomes more complicated, with the introduction of inhomogeneity and multiple fluid phases, Darcy's law is extended, to the Darcy-Buckingham equation and eventually Richard's equation, in an attempt to predict the fluid movement. Darcy-Buckingham equation expands Darcy's equation for unsaturated porous media, where the permeability is dependent on the saturation (S_w). Richard's equation, Equation 2, is then established by combining the Darcy-Buckingham equation with the conservation of mass equation.

$$\frac{dS_w}{dt} = \frac{\partial}{\partial x}\left(\frac{\kappa(S_w)A}{\mu}\frac{\partial P}{\partial x}\right) + \frac{\partial}{\partial y}\left(\frac{\kappa(S_w)A}{\mu}\frac{\partial P}{\partial y}\right) + \frac{\partial}{\partial z}\left(\frac{\kappa(S_w)A}{\mu}\frac{\partial P}{\partial z}\right) \qquad \text{Equation 2}$$

However, even Richard's equation is unable to capture many of the phenomena that influence multi-phase flow. Thus, there is a need to develop a more robust model that can produce accurate predictions of subsurface flow.

An important part of multi-phase flow systems is represented by the relationship between capillary pressure (P_c) and saturation. However, this relationship is not completely defined, and there is an element of hysteresis. The capillary pressure-saturation relationship is dependent on the porous medium and the history of flow, causing each capillary pressure-saturation relationship to be unique for every multi-phase flow system. For each saturation, there is a possibility for many different fluid configurations allowing for even more variability in the relationship. A thermodynamically based theory presented by Hassanizadeh & Gray, 1993 suggests that interfacial area (a_{nw}) could be included to create a fully defined relationship for each system. Interfacial area provides a way to specify the fluid configuration at each saturation point by relating the systems energetics and fluid content.

Using X-ray computed microtomography, high-resolution non-destructive three-dimensional images of porous media systems can be created, allowing for the accurate measurement of interfacial area and capillary pressure, from curvatures, as fluid configuration changes over time. Hassanizadeh & Gray, 1993 theory has been validated for two-phase flow both with a two-dimensional micromodel (Chen et al., 2007), and for three-dimensional systems (Porter et al., 2009), when capillary pressure-saturation-interfacial area surfaces were shown to be unique, eliminating hysteresis.

However, when a third phase is introduced the system becomes significantly more complicated. There are three saturations; air (S_a), oil ($S_{o)}$, and water ($S_{w)}$, three capillary pressures; air-water ($P_{c,a\text{-}w}$), air-oil ($P_{c.a\text{-}o}$), and oil-water ($P_{c,o\text{-}w}$), and three interfacial areas; air-water ($a_{a\text{-}w}$), air-oil ($a_{a\text{-}o}$), and oil-water ($a_{o\text{-}w}$). Traditional three-phase models are extensions of two-phase models. These models are not able to capture fully the phenomena that occur when all three phases occupy the same pore, due to differences in the saturation paths and the movement of hydraulically disconnected phases. The objective of this study is to determine, experimentally, whether each of the phase pairs can be defined via a capillary pressure-saturation-interfacial area relationships, thus allowing us to establish a more robust model describing three-phase flow, including hysteresis. Specifically the goals are to determine if the interaction of each fluid pair of our three-phase system will be uniquely defined by a capillary pressure-saturation-interfacial area surface, eliminating hysteresis. As well as, to understand the

effect altering the wettability of the media will have on the capillary pressure-saturation-interfacial area surfaces created.

2 Background

2.1 Wettability

Porous media flow is the flow of fluids through a solid matrix consisting of a series of pores connected by smaller throats. Wettability of the solid matrix plays a large role in determining fluid distributions in the system. Typically, wettability is determined based on the distribution of contact angles throughout the matrix. When the solid-water contact is less than 90 degrees, the system is considered water-wet, and at greater than 90 degrees, the system is oil-wet. Most natural rocks are water-wet, but can become oil-wet when polar substances attach to the surface, altering the contact angle, for instance via prolonged exposure to hydrocarbons.

It is unlikely that the system will be wetted the same in all locations. There are two types of non-uniform wettability matrices, mixed-wet and fractionally-wet. A mixed-wet system can be defined in two ways, by varying wettability in a single pore, where the corners and crevices are water-wet and the bulk center of the pore is oil-wet (Helland & Skjaeveland, 2007; Helland & Skjaeveland, 2006; Hui & Blunt, 2000; Singh et al., 2016; Spiteri et al., 2008), or variation over the matrix where the larger pores are oil-wet and smaller pores are water-wet (Holm et al., 2010; van Dijke et al., 2001; van Dijke & Sorbie, 2002; van Dijke et al., 2004). A system that is fractionally-wet occurs when a portion of the grain surfaces are water-wet and a portion of the surfaces are oil-wet (Armstrong & Wildenschild, 2012; Bradford & Leij, 1996). In this study, we will be looking at a water-wet system and a fractionally-wet system.

In a three-phase system there exists a wetting phase, a non-wetting phase, and an intermediate-wetting phase. The wetting phase typically fills the smallest pores and throats as well as forming the wetting layers, the non-wetting phase fills the largest pores, and the intermediate-wetting phase fills the intermediate-sized pores. Table 1 shows the typical wetting order for systems with differing wettabilities.

Table 1: Wetting Order

Wetting Order	**Wetting**	**Intermediate-Wetting**	**Non-Wetting**
Water-Wet	Water	Oil	Gas
Strongly Oil-Wet	Oil	Gas	Water
Weakly Oil-Wet	Oil	Water	Gas

Weakly oil-wet systems occur when the oil-water and gas-water contact angles are both less than 90 degrees. Figure 1, depicts potential fluid configurations in a single pore with differing wettabilities.

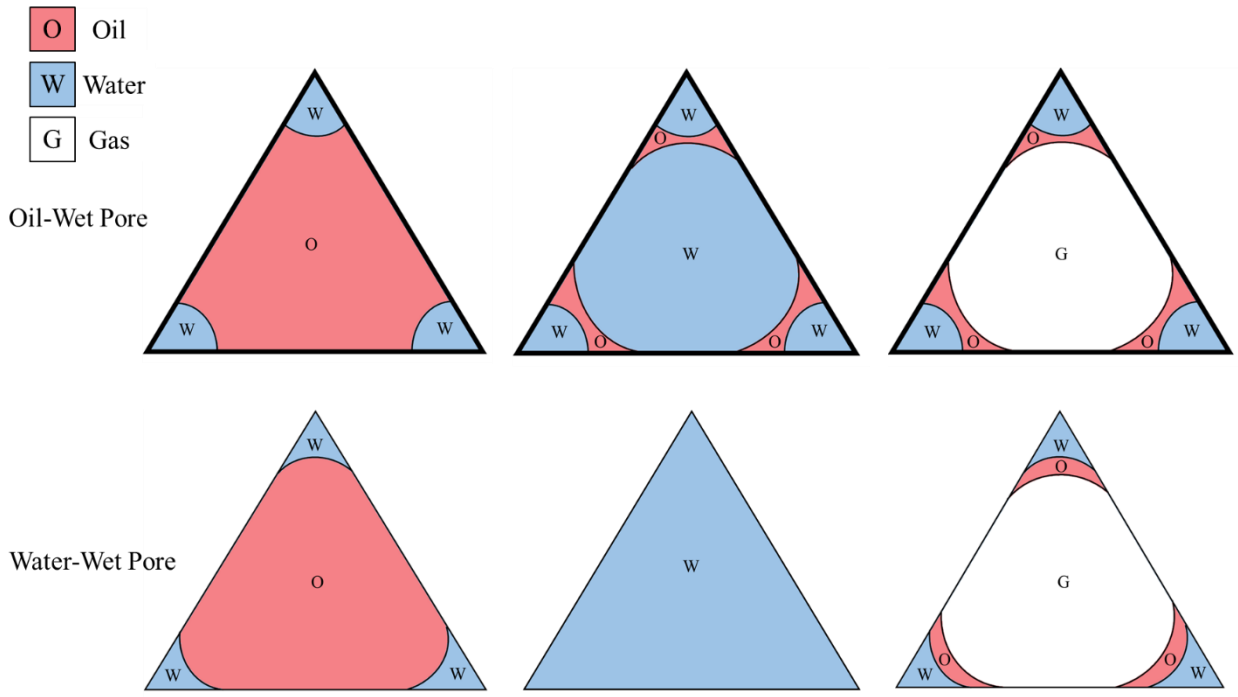

Figure 1: Potential fluid configurations in a single pore for two- and three-phase flow. Bold lines represent oil-wet solid surfaces. Figure adapted from (Blunt, 2001).

Three-phase wettability cannot be described like two-phase wettability. This is to some degree because in the presence of an intermediate phase, oil, spreading films may develop

between the wetting and non-wetting phases. The extent to which oil layers are formed depends on the spreading coefficient of the oil. The spreading coefficient (C_s) is derived from the interfacial tensions between the three fluid phases in Equation 3.

$$C_s = \sigma_{gw} - (\sigma_{ow} + \sigma_{go}) \quad \text{Equation 3}$$

Where σ_{gw} is the interfacial tension between the gas and water phases, σ_{ow} is the interfacial tension between the oil and water phases, and σ_{go} is the interfacial tension between the gas and the oil phases. Interfacial tension is defined as the change in free energy (F) over the change in area (a) of the surfaces between the phases, and is shown in Equation 4.

$$\sigma = \frac{dF}{da} \quad \text{Equation 4}$$

If the spreading coefficient is positive then the oil is spreading, and if the spreading coefficient is negative, the oil is non-spreading. Spreading oils, for instance Soltrol220, will form stable layers that are able to swell between the water and gas phases in the system. Non-spreading oils, for instance decane, will form thin films between the water and gas phases only because they are the intermediate-wetting phase. However, these films are unstable and have a limit to their thickness, after which the oil will form droplets.

Three-phase wettability is typically only defined by the oil-water contact angle. With knowledge of the oil-water contact angle (θ_{ow}) and the interfacial tensions (σ), all other contact angles can be determined analytically. Equation 5 defines the gas-water contact angle (Blunt, 2017).

$$cos\theta_{gw} = \frac{1}{2\sigma_{gw}}[(C_s + 2\sigma_{ow})cos\theta_{ow} + C_s + 2\sigma_{go}] \quad \text{Equation 5}$$

Equation 6, the Bartell-Osterhof equation, determines the gas-oil contact angle.

$$\sigma_{gw}cos\theta_{gw} = \sigma_{ow}cos\theta_{ow} + \sigma_{go}cos\theta_{go} \quad \text{Equation 6}$$

The Equations 5 and 6 above are valid at equilibrium with fluids at rest.

2.2 Capillary Pressure

The main driving force for flow is pressure differences across the matrix at the Darcy scale, and at the pore scale the capillary pressure. Capillary pressure is defined as the pressure difference between two immiscible fluids that form an interface with each other shown in Equation 7.

$$P_c = P_{nw} - P_w \qquad \text{Equation 7}$$

Where P_c is the capillary pressure, P_w is the pressure of the wetting phase, and P_{nw} is the pressure of the non-wetting phase. The capillary pressure can also be calculated based on the geometry of the meniscus at the interface between the fluids via the Young-Laplace equation, Equation 8.

$$P_c = 2\sigma * \frac{\cos(\theta)}{r} = \frac{2\sigma}{R} \qquad \text{Equation 8}$$

Where σ is the interfacial tension between the two fluids, r is the radius of the capillary tube, R is the radius of curvature, and θ is the contact angle. The geometric variables used in the Young-Laplace equation are shown in Figure 2 representing a capillary tube.

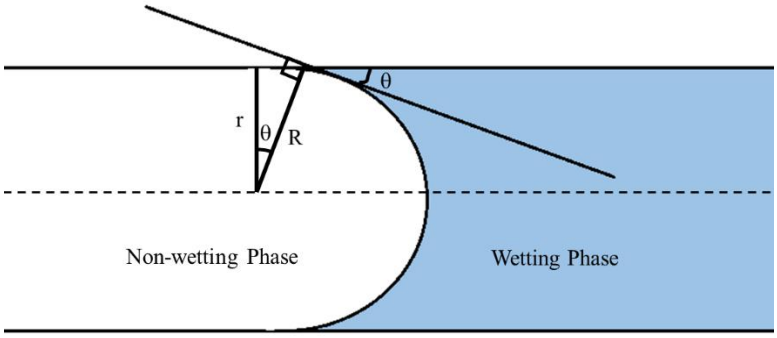

Figure 2: Capillary tube geometry

In a capillary tube, the meniscus is spherical and regular so there is only one radius of curvature, however, in porous media, the interfaces between fluids are not regular and have two principal

radii. For simplification, the mean curvature, H, is used in calculating capillary pressures using the Young Laplace equation, Equation 9.

$$P_c = 2\sigma H \qquad \text{Equation 9}$$

2.3 Drainage vs Imbibition

Porous media multi-phase flow is typically classified as either two- or three-phase flow, where each phase is a different immiscible fluid. There are two types of displacement for two-phase flow, imbibition and drainage. Imbibition occurs when the wetting fluid is replacing the non-wetting fluid. In imbibition, common theory suggests that the pore with the highest threshold capillary pressure is invaded regardless of location because it is assumed that the wetting phase is connected throughout the matrix. In an individual pore, there are two methods for the displacement of fluids during imbibition, snap-off and piston-like displacement, shown in Figure 3. Snap-off occurs when, the capillary pressure decreases and the curvature of the fluid interface changes causing a swelling of the wetting phase in the corners of the pore. As the swelling increases, the non-wetting fluid loses contact with the surface of the matrix and the pore then spontaneously fills with the wetting fluid, or the non-wetting fluid becomes trapped in the center of the pore. Piston-like displacement occurs when the wetting phase invades a pore or throat that is filled with the non-wetting phase. Piston-like displacement is a more likely displacement method because it can occur at higher capillary pressures, however piston-like displacement can only occur if adjacent pores are filled with the wetting phase.

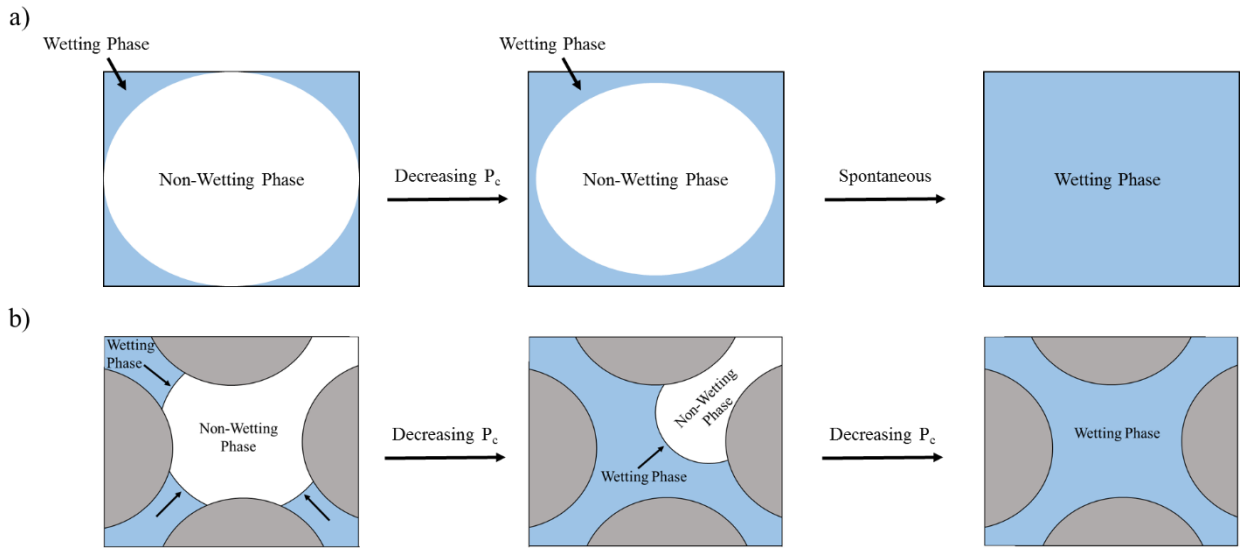

Figure 3: Image of individual pore displacement techniques a) Snap-off and b) Piston-like

Drainage occurs when the wetting fluid is being replaced by the non-wetting fluid. Drainage can only proceed via piston-like displacement, where the adjacent pore with the lowest threshold capillary pressure is invaded. In a three-phase system, flow becomes more complex because of the intermediate-wetting fluid. Displacement can occur as double displacement; where one fluid displaces another which then displaces the third. The main mechanisms for the movement of the fluid in an individual pore are the same as in two-phase flow.

On a macroscopic scale, flow is classified via flow regimes, which can be used to understand the forces dominating flow, either viscous or capillary. During drainage, there are three types of displacement, defined for two-phase flow, viscous fingering, capillary fingering, and stable displacement (Lenormand et al., 1988). The different displacement patterns are governed by the capillary number (C_a), the ratio between viscous forces and capillary forces, and the mobility ratio (M), the viscosity ratio between the fluids. In stable displacement, the pattern is a flat front, and the driving force for flow is mostly due to the viscosity of the injected fluid. For viscous fingering, the main driving force is the viscosity of the displaced fluid, creating fingers that spread only in the flow direction. In capillary fingering, the viscous forces are negligible and capillary effects control flow, the fingers again spread across the network growing

in all directions. The Lenormand phase diagram can be used to determine the flow pattern for each system, Figure 4.

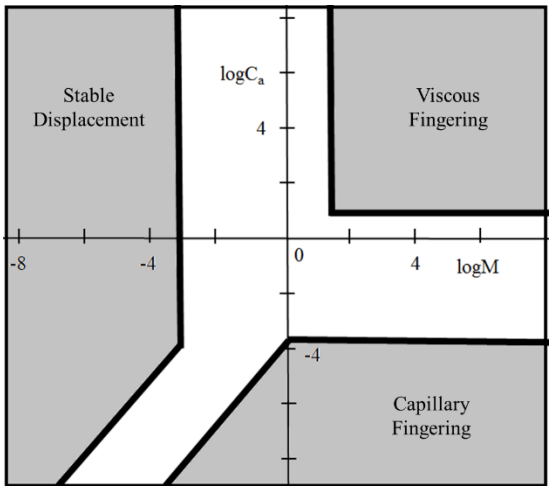

Figure 4: Lenormand Phase Diagram

When considering imbibition, the number of macroscopic displacement patterns increases due to the inclusion of snap-off as a pore scale displacement process. These displacement patterns are determined based on the contact angle, capillary number, and initial wetting phase saturation. Imbibition patterns for low initial wetting phase saturation are bond percolation, flat frontal advance, and compact cluster growth, for high initial wetting phase saturation there are ramified cluster growth, and dendritic frontal advance (Hughes & Blunt, 2000). Bond percolation is displacement where throats fill in order of size, dominated by snap-off causing a significant amount of trapping. In full frontal advance, piston like displacement dominates, and causes a front, like in stable displacement. For compact cluster growth, snap-off occurs in very small throats and the surrounding pores are invaded via a piston-like mechanism. Ramified cluster growth occurs when there is a large initial wetting phase saturation, the initially filled pores are sites for clusters to grow creating a more ragged shape than the compact clusters. Finally, dendritic frontal advance occurs when piston-like displacement dominates, but the

presence of a high initial wetting phase saturation causes more trapping via the bypassing of pores. Figure 5 depicts phase diagrams for imbibition displacement patterns.

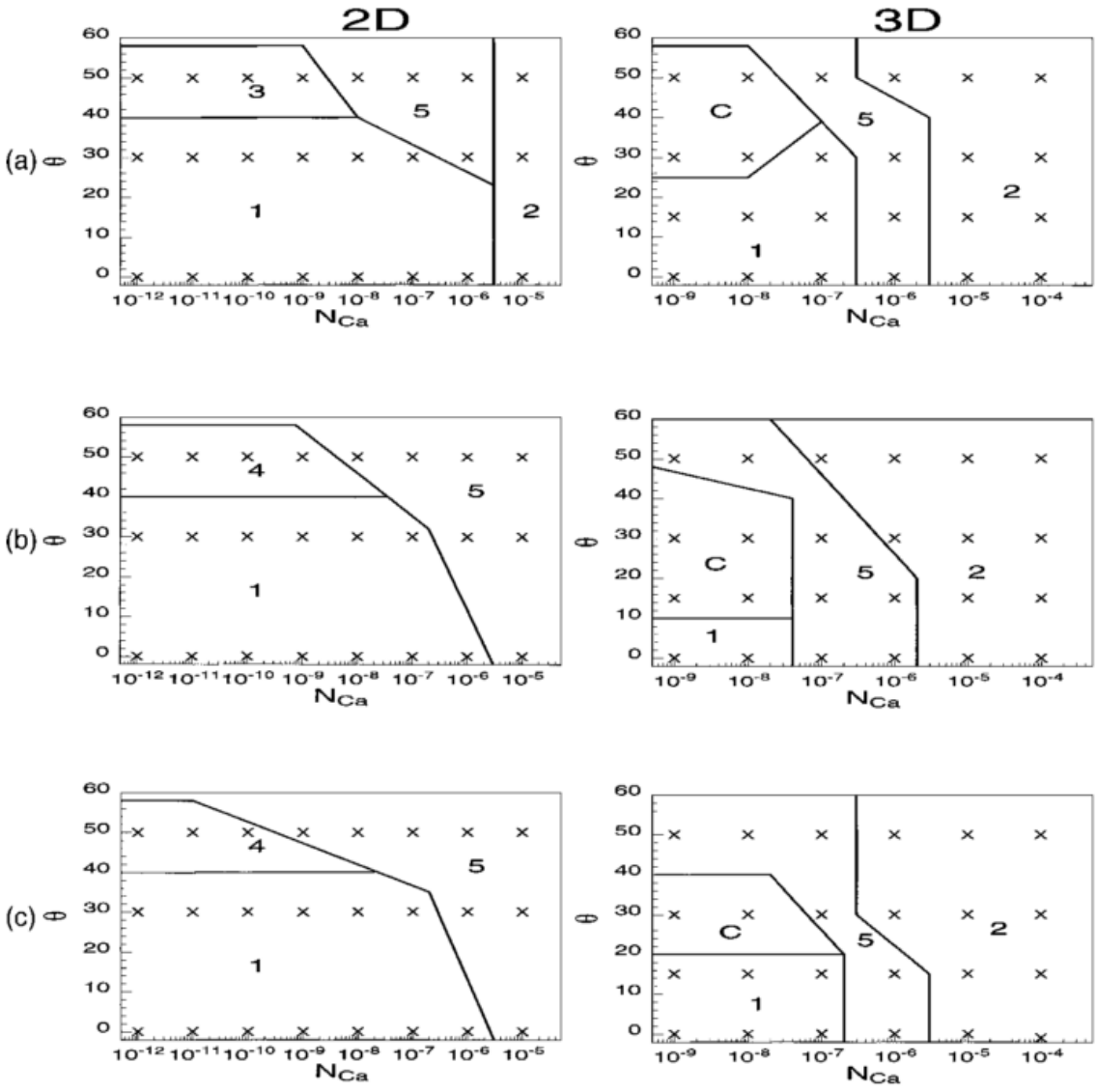

Figure 5: Phase diagrams for imbibition displacement patterns. The left column is for two-dimensional simulations and the right column is for three-dimensional simulations. Regime 1 is bond percolation, 2 is flat frontal advance, 3 is compact cluster growth, 4 is ramified cluster growth, 5 is dendritic frontal advance, C is cluster growth for three-dimensional simulations. Initial wetting phase saturation for a) S_w = 0%, b) S_w = 8%, c) S_w = 15% (Hughes & Blunt, 2000)

2.4 Capillary Pressure-Saturation Curves

Multi-phase flow in porous media is often described by the capillary pressure-saturation relationship. The saturation of a fluid is defined in Equation 10.

$$S_i = \frac{Volume\ of\ Fluid\ i}{Total\ Fluid\ Volume} \qquad \text{Equation 10}$$

Typically, capillary pressure-saturation curves are displayed with the wetting phase saturation on the x-axis and capillary pressure on the y-axis. When dealing with more than two fluid phases a different capillary pressure-saturation curve is needed for the capillary pressure between each of the three phases. During drainage, wetting phase saturation decreases as capillary pressure increases, and the opposite is true during imbibition. An example of a two-phase pressure saturation curve can be seen in Figure 6.

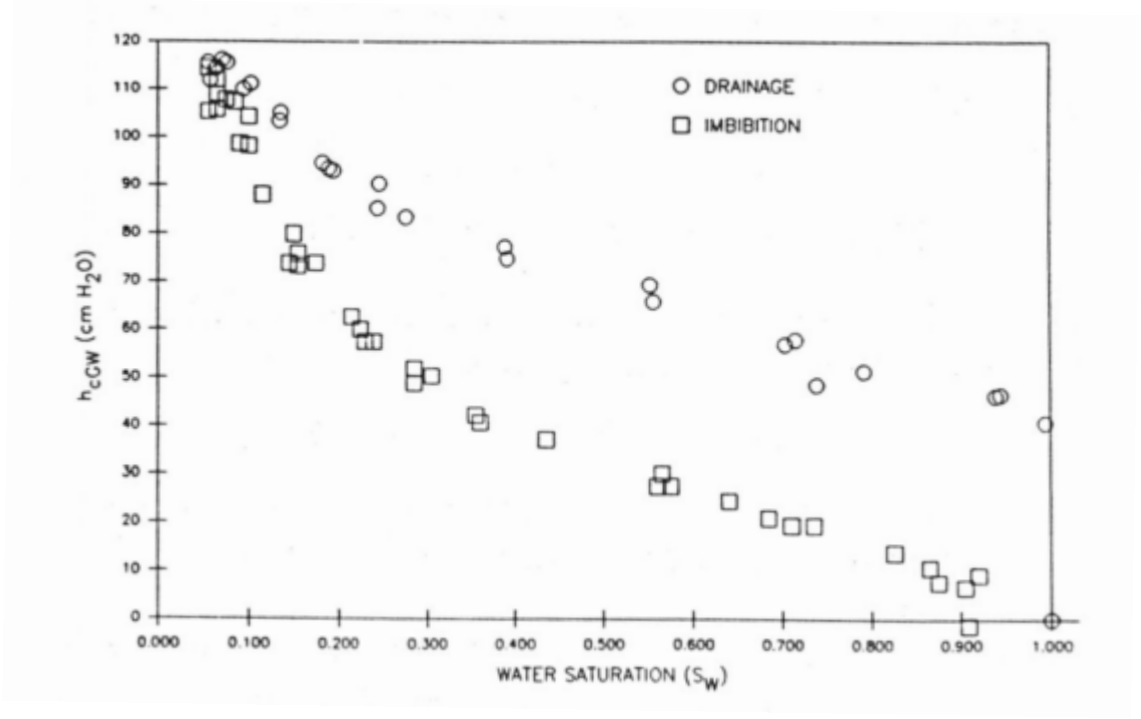

Figure 6: Capillary Pressure Saturation Curve for Two-Phase Data (Ferrand et al., 1990)

The distinct separation of the drainage and imbibition curves is due to hysteresis. One reason for hysteresis in the capillary pressure-saturation relationship is the non-uniformity of pore size. The ink bottle effect can be used to explain this phenomenon, Figure 7. From the Young Laplace equation, Equation 8, the capillary pressure is inversely proportional to the radius. Since R is greater than r, $P_{c,R}$ is less than $P_{c,r}$, therefore a lower capillary pressure is required to imbibe rather than drain the same pore.

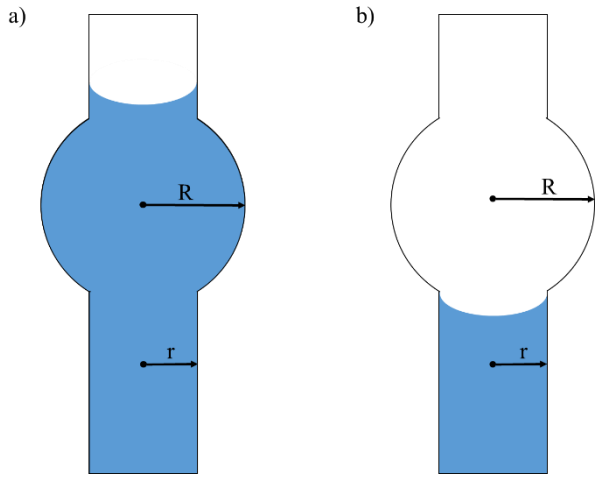

Figure 7: Ink-Bottle Effect a) drainage b) imbibition

Additionally, contact angle hysteresis affects the hysteresis in the capillary pressure-saturation relationship. Again, from the Young-Laplace equation, the threshold capillary pressure for a pore decreases as the contact angle increases. The capillary pressures for imbibition are lower than drainage because the advancing contact angle is larger than the receding contact angle. Contact angle hysteresis is exemplified with a droplet of water running down an inclined glass surface, Figure 8.

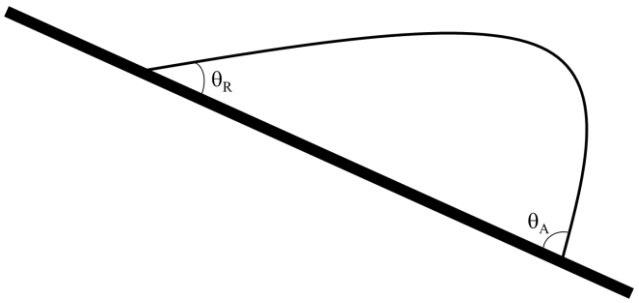

Figure 8: Raindrop effect: advancing and receding contact angles

2.5 Surface Free Energy

When looking at the interface between fluids mathematically, they are typically described as a Gibbs surface. A Gibbs surface is a nonhomogeneous film separating two homogeneous bulk phases. The size and extent of the film is dependent on the surface tension between the fluids. Surface tension is the force exerted on the interface due to the attraction of the molecules in the film towards their bulk phase. In fluids, surface tension is independent of direction and so can be simply measured as a constant value. Numerically, surface tension is defined as the reversible work of extension/formation per unit area of surface. When discussing fluid interfaces the surface free energy per unit area, f_s, becomes important (Morrow, 1970). Surface free energy is shown in Equation 11.

$$f_s = \sigma \Delta A \qquad \text{Equation 11}$$

For non-spreading fluids the work done, on or by the system, is used to move the interface of the bulk liquids. During drainage, work is done on the system, increasing the surface free energy and therefore the interfacial area, and during imbibition, work is done by the system decreasing the surface free energy and interfacial area. Throughout a reversible and smooth flow process, all the work done is converted into surface free energy. However, the presence of hysteresis in porous media flow shows that it is not a reversible process. A source of the irreversibility in flow through porous media is known as Haines jumps. This occurs when capillary pressure does not change smoothly with change in saturation, and is due to unstable fluid configurations. When Haines jumps occur, free energy of the system is lost. Typically this

energy is lost as heat, which is able to quickly equilibrate, causing the overall temperature change in the system to be negligible (Morrow, 1970).

2.6 Microtomography

X-ray computed microtomography is a technique to generate high-resolution three-dimensional images of the internal structure of a sample in a non-destructive manner. In radiographic imaging, a two-dimensional projection of the three-dimensional object is produced. However, using computed tomography, the sample is rotated and an image is acquired at multiple angles. The series of two-dimensional projections are then reconstructed and combined to generate a three-dimensional image of the object's internal structure.

Figure 9 illustrates the basics of synchrotron-based imaging.

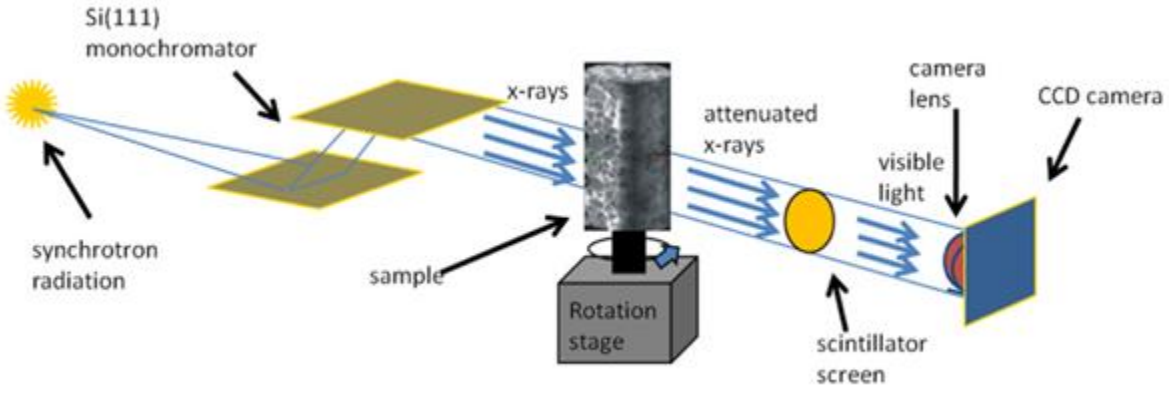

Figure 9: X-ray Microtomography Set-up (Wildenschild & Sheppard, 2013)

X-rays are bounced off a monochromator, to ensure only x-rays of a specific energy are used. The x-rays are then transmitted through the sample and a fraction are attenuated. After passing through the sample, the x-rays interact with a scintillator that converts them to visible light, and an image is therefore captured by the camera.

Synchrotron radiation is electromagnetic radiation, created via a high-speed particle accelerator. The electrons are then slowed down with large electromagnets resulting in x-ray emission. As these x-rays hit the sample, they are attenuated. X-ray attenuation is the reduction of the intensity of the x-ray beam as it passes through matter. This reduction can be caused by either absorption or deflection of the photons in the x-ray beam. The intensity of the x-rays after they have passed through a sample can be determined using Beer-Lamberts Law, Equation 12 (Mcketty, 1998).

$$I = I_o e^{-\mu x} \qquad \text{Equation 12}$$

I_o is the initial beam intensity, I is the attenuated beam intensity, x is the thickness of the sample, and μ is the attenuation coefficient. The attenuation coefficient is the change in intensity of the x-ray beam per thickness of the sample. Factors affecting the attenuation coefficient include beam energy, bulk density of the sample, and atomic number of the sample.

Water and oil that are used in multi-phase flow experiments have very similar attenuation coefficients, however, a heavier contrast agent can be added to alter their attenuation properties. Figure 10 shows a plot of how the attenuation coefficient for different materials changes with beam energy.

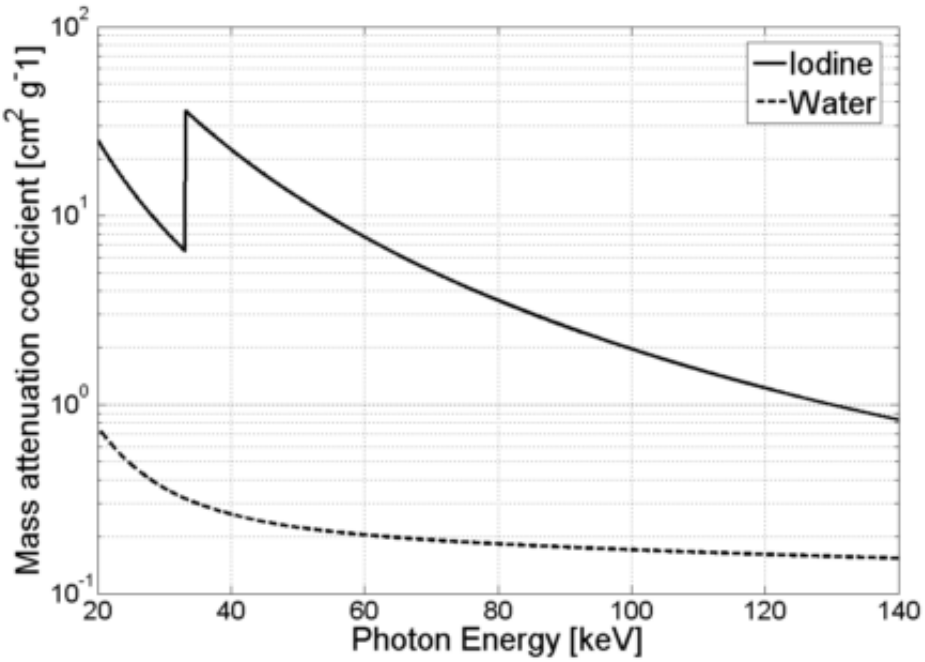

Figure 10: Mass attenuation coefficient for iodine and water versus beam energy (Burton et al., 2015)

The sharp peak that can be seen for the iodine is called the k-edge. The k-edge is the photoelectric absorption edge, where the binding energy of the photon is above that of the binding energy of the k-shell electron. At this energy, the x-ray photons more easily absorb to the material causing a sudden increase in attenuation. By adding iodine at different concentrations to both the water and the oil, and imaging at one energy, above the k-edge for iodine, a greater contrast can be seen between the materials. When converted to visible light, and reconstructed, the materials with the highest attenuation appear brightest, and those with little attenuation appear very dark. Air is assumed to have little to no attenuation and so appears to be the darkest phase in the resulting images.

3 Literature Review

Multi-phase flow in porous media is a field that has been extensively studied. There are a myriad of experimental results and models to help better understand subsurface multi-phase flow. Throughout these studies, a consistent component of modeling fluid flow behavior was developed based on capillary pressure-saturation curves. Any attempt to perform a numerical simulation on a multi-phase flow system will be starting from this relationship. Many of the studies performed on porous media have led to the same conclusion, that capillary pressure is not uniquely dependent on the saturation of the system, but it is also dependent on the saturation history of the system, thus introducing the concept of hysteresis (Fenwick & Blunt, 1998; Lenhard, 1992).

The inherent hysteresis in porous media systems has made it difficult to create models of flow in such systems. The failure of the capillary pressure saturation curves to uniquely describe drainage and imbibition in multi-phase systems led Hassanizadeh & Gray, 1990 to reexamine how we describe porous media flow from a thermodynamic perspective. They developed an extended form of Darcy's Law using momentum balance equations determining that capillary pressure was a function of more than saturation, but had an interfacial area dependence as well (Hassanizadeh & Gray, 1990). They then took their model to the next step by mathematically predicting that the traditional hysteresis seen in the Pc-S relationship is actually a projection of the capillary pressure-saturation-interfacial area surface onto the capillary pressure-saturation plane (Hassanizadeh & Gray, 1993). The model that Hassanizadeh & Gray, 1993 created was then expanded to show that the model was fully defined when using either interfacial area or common lines as the third variable (Held & Celia, 2001). However, there was still no reliable way to determine interfacial area and common line lengths in physical experiments.

3.1 Experimental Technique

A new imaging technique, X-ray computed microtomography, can produce high-resolution non-destructive three-dimensional images of porous media systems and the fluids within them (Blunt et al., 2013; Wildenschild & Sheppard, 2013). Due to inherent resolution limitations microtomography approaches the smooth sphere ideal and it is not possible to track

features, and therefore interfacial areas that are due to surface roughness and micro-porosity (Brusseau et al. 2006). However, with careful image processing techniques the interfacial surfaces associated with capillary dominated flow (i.e. not film flow) can be preserved if imaged at a sufficiently high resolution (Culligan et al., 2004; Wildenschild & Sheppard, 2013). In recent years it has also become possible to measure curvatures the same interfacial surfaces, which can then be used in determining capillary pressures via the Young-Laplace equation (Armstrong et al., 2012; Li et al., 2018).

3.2 Two-Phase Flow Experiments

Using advanced experimental techniques, many two-phase flow experiments have been performed to test Hassanizadeh & Gray, 1990 theory. In a two dimensional etched lithography micromodel capillary pressure-saturation-interfacial area surfaces have been shown to be unique for a given system, eliminating hysteresis (Chen et al. 2007). Similarly, using three dimensional x-ray microtomography Porter et al., 2009 verified the two-dimensional findings and also showed that due to the non-hysteretic nature of the capillary pressure-saturation-interfacial area surface, scanning curve data is not required to describe the relationship (Porter et al., 2009). The surface created by the three state variables can then be fitted with a biquadratic polynomial, and is smooth on the continuum scale (Porter et al. 2010; Reeves & Celia, 1996). With the understanding of the importance of interfacial area as a state variable in defining a system, additional models have been developed, including one able to predict the interfacial area-saturation relationship from the capillary pressure-saturation relationship and pore size distribution (Diamantopoulos et al., 2016), and using the capillary pressure-saturation-interfacial area surface to model interfacial areas for non-equilibrium systems (Joekar-Niasar & Hassanizadeh, 2012).

A logical next step is to generate experimental justification that a system can be fully defined with the addition of interfacial area for three-phase flow systems as well. A traditional method of extending three-phase flow has been to expand two-phase capillary pressure equivalents (Kantzas et al., 1998), however, if all three phases in a system are in contact in the same pore this affects all the capillary pressures and the system can no longer be modeled using

a two-phase capillary pressure relationship (Piri & Blunt, 2004). These differences are caused by differences in the saturation paths between two-phase and three-phase conditions. The differences are small for water-wet systems, but are larger in systems with different wettability (van Dijke & Sorbie, 2004). Another reason that two-phase flow models cannot be used to predict three-phase flow is that the models are often based on Darcy's law, which is not valid in three-phase flow due to movement of phases that are not hydraulically connected (van Dijke et al., 2004). Finally when using two-phase flow data, surface tensions are only scalable during strict drainage scenarios, and not when imbibition is involved (Ferrand et al., 1990). This means three-phase experiments must be performed to see if Hassanizadeh & Gray, 1990 theory is still valid with the addition of another fluid.

3.3 Fluid Phase Interactions

Interactions between the fluid phases is likely to play a major role in how fluid moves through a porous medium. It has been shown that in a two-phase system a capillary pressure-saturation curve for any fluid pair can be predicted from one fluid pair using a relationship between the interfacial tensions (Lenhard & Parker, 1987). This means that the types of fluids in a porous medium system can affect the displacement mechanisms as much as the characteristics of the pore space itself. Three-phase flow models that fail to consider interfacial coupling often result in significant errors in their predictions (Bentsen & Trivedi, 2012). Errors seen when ignoring interfacial characteristics most likely occur due to the conversion of work to surface free energy in the form of interfacial area, and energetics must be characterized in the models. Morrow, 1970 showed that the area under the capillary pressure curve is the external work of the system, and that the area of the hysteresis loop is the minimum amount of work lost to heat (Morrow, 1970). A two-phase experiment showed that in a sphere pack, an 85% efficiency of work converted to surface free energy could be achieved (Seth & Morrow, 2007). Introducing an additional fluid phase into the flow system often involves films and will most likely have a significant effect on efficiency of work conversion and thus fluid phase distributions.

3.4 Wettability

As mentioned previously, the wettability of the system also has a great impact on fluid displacement in porous media. Simulations have shown that wettability affects fluid displacements even when capillary pressure effects are removed from the system (Holm et al., 2010). Changing the wettability of the system has a large effect on flow characteristics and the types of displacement that occur in two-phase flow (Al-futaisi & Patzek, 2003), and it is reasonable to believe that the same effects will be seen in three-phase flow. The presence of three fluid phases in the system does not affect the wettability characteristics of each fluid pair, which is wetting vs. non-wetting, but the addition of a third phase introduces an intermediate-wetting phase (Khishvand et al., 2016). A more oil-wet medium reduces the residual oil saturation and increases the critical capillary number of the system by stabilizing the oil invasion through cooperative pore filling (Caubit et al., 2004; Holtzman & Segre, 2015; Humphry et al., 2014). Additionally in two-phase systems, oil-water interfacial areas are affected by wettability. Simulations have shown that in a water-wet system the maximum specific interfacial area, in primary drainage, occurs between 0.2-0.35 water saturation, whereas in an oil-wet system the maximum occurs between 0.7-0.8 water saturation (Raeesi & Piri, 2009). Experimental results confirm the simulations for a water-wet system (Porter et al., 2010; Raeesi & Piri, 2009), however to the best of our knowledge there is no experimental data on interfacial area in oil-wet systems.

In three-phase flow, the intermediate-wetting phase often forms films separating the wetting and non-wetting fluids, even more significantly affecting fluid interfacial areas. The profound and widespread affect that the wettability of the system has on the flow characteristics of the system leads to the prediction that altering the wettability will greatly affect the relationship between capillary pressure, saturation, and interfacial area of the system.

4 Methods

4.1 Materials

To create a simplified porous medium matrix, a mixture of soda lime glass beads were placed in a glass column (water-wet system: height 45 mm, inner diameter 5 mm, fractionally-wet system: height 35 mm, inner diameter 6 mm). Using this manufactured porous medium as opposed to core samples of real rock allows for complete control over the wettability characteristics of the medium as well as allowing for more consistent physical properties, (porosity, mineralogy, permeability etc.) between successive experiments. The glass beads are naturally water-wet, however for part of the study, the wettability of the beads was altered, so some experiments were conducted using a water-wet system, and some with a fractionally-wet system. The glass bead mixture used in each experiment is described in Table 2 as weight percent. In the fractionally-wet system, the largest sized beads, 1000 μm-1400 μm, were oil-wet and the two smaller sizes were water-wet, resulting in 65% of the total surface area being oil-wet.

Table 2: Bead Pack Characteristics

Water-Wet System		Fractionally-Wet System	
Bead Diameter	Weight Percent	Bead Diameter	Weight Percent
650 μm	35%	650 μm	26%
800 μm	35%	850 μm	26%
1000-1400 μm	30%	1000-1400 μm	48%

The fluids used in the system were water, air, and decane. Decane is a non-spreading oil (negative spreading coefficient) with a density of 0.73 g/ml. The interfacial tensions of the fluid pairs can be found in Table 3.

Table 3: Fluid Interfacial Tensions

Fluid Interactions	Interfacial Tension (dyne/cm)
Water/Air (Agrawal & Menon, 1992)	72.75
Water/Decane (Zeppieri et al., 2001)	52.33
Air/Decane (Rolo et al., 2002)	24.47

In order to improve the image contrast between the water, air, and oil, contrast agents were added. A brine solution was created by mixing potassium iodide (KI) and water at a weight ratio of 1:6, similarly iodobenze was added to decane at a weight ratio of 1:24. The difference in iodine concentration was sufficient to distinguish water from decane. Imaging was performed at an energy slightly above the iodine edge, providing significant contrast between the phases and thereby allowing for easier segmentation during image analysis.

4.2 Wettability Altering Procedure

A silanization process was used to treat the surface of the glass beads to change the wettability. A three-step process occurs when using octadecyltrichlorosilane (OTS) to treat glass surfaces. First is a hydrolysis of the chlorinated portion of the OTS molecule generating silanetriol at the surface, then the silanetriol attaches to the surface through hydrogen bonding, and finally a Si-O-Si covalent bond forms on the glass surface (Mcgovern et al., 1994). The beads were first soaked in a solution of 5% OTS and 95% toluene by volume, for 24 hours, then rinsed with both toluene and nanopure water to remove the OTS films from the bead surfaces (Armstrong & Wildenschild, 2012). Clean glass slides were treated in the same batch as the beads so that the contact angle of the treated surfaces could be determined and used to quantify the surface wettability modification. An FTA 32 goniometer was used to generate the contact angle measurements. An 8 μl drop of reverse osmosis water was placed on the glass slide, and

an image was acquired using a microscope. The surface of the drop was then selected and the contact angle determined as shown in Figure 11.

a) b)

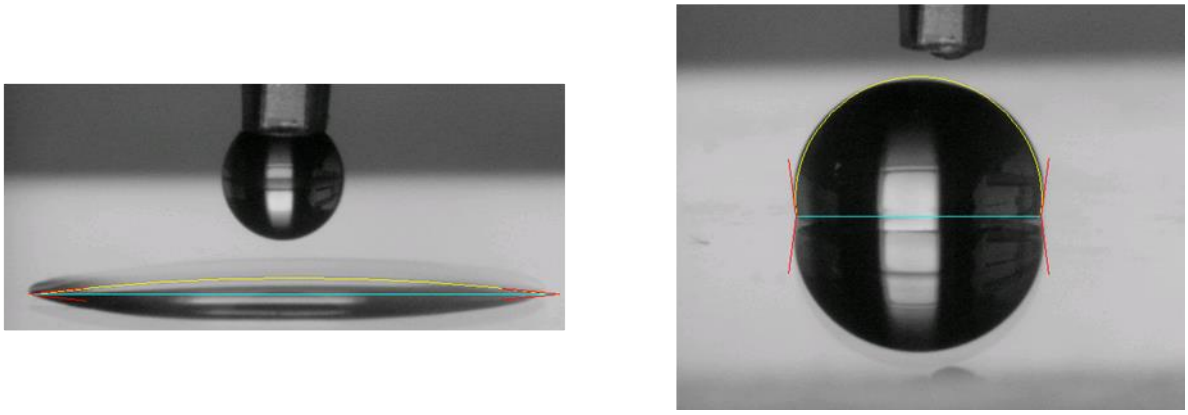

Figure 11: Contact Angle Measurement a) untreated slide b) treated slide

Four different slides were tested for both treated and untreated, with three measurements collected on each slide. The contact angles measured are reported in Table 4.

Table 4: Contact Angle Measurements

Sample	Contact Angle	Standard Deviation
Untreated	8.31°	1.79°
Treated	100.95°	2.91°

4.3 Fluid Flow Experimental Set-up

The bead-filled column was mounted in a sample holder with a semi-permeable membrane on both ends. The bottom membrane is hydrophilic (MAGNA, 1.2 μm) allowing only water to enter and exit the column. The membrane at the top of the column is hydrophobic (Pall Corporation PTFE, 0.45 μm) allowing only oil to pass through, blocking both water and air.

There are two air vents located on the sides of the column allowing air to enter or leave when open. Flow is controlled via the water lines connected to the bottom of the column using a syringe pump that either injects water into the system (imbibition) or pulls water out of the system (drainage). The resulting changes in pressure caused by the movement of the pump, and thus the water phase, leads to the movement of the other mobile fluids in the system. Using the syringe pump the flow rates remained low keeping the system at a quasi-static state. Figure 12 below is a schematic of the experimental set-up and sample holder.

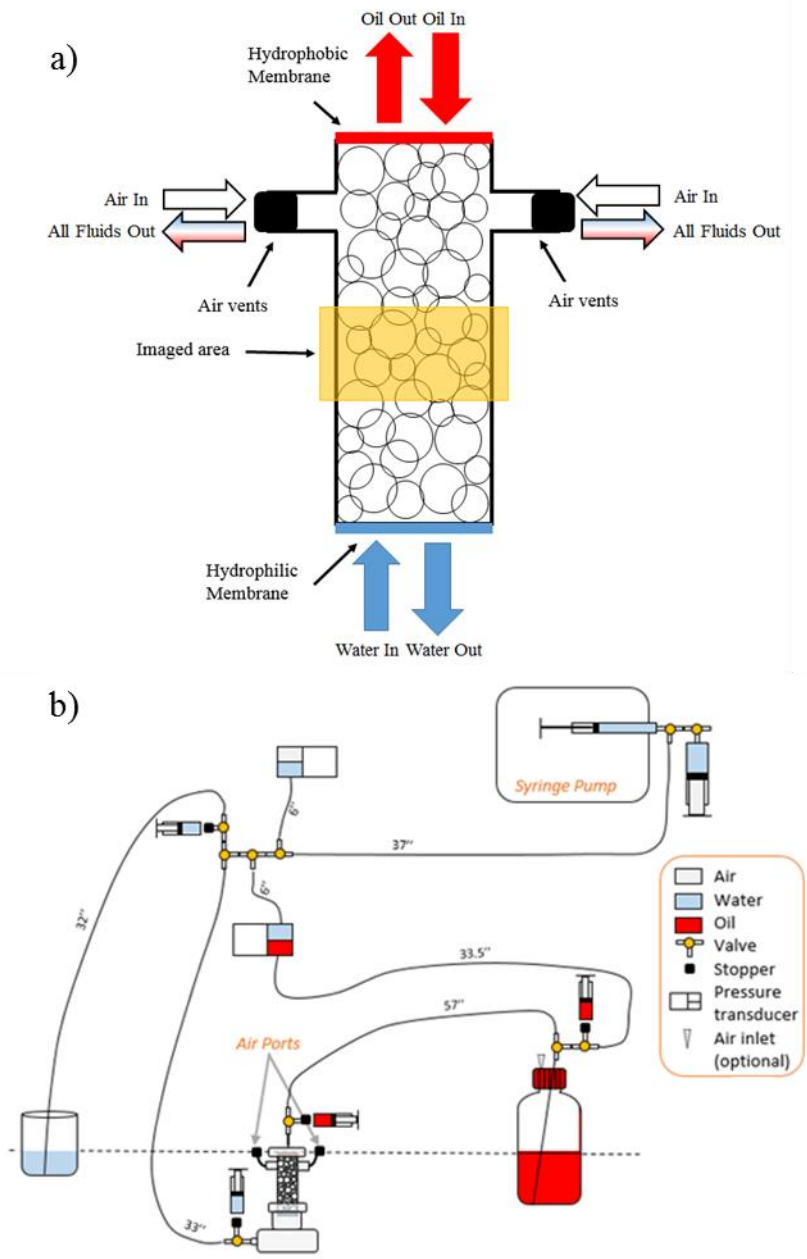

Figure 12: a) Schematic of Sample Holder b) Schematic of Entire Experimental Set-up

4.4 Fluid Flow Experimental Procedure

The objective of this experiment was to capture the fluid configurations from a flow scheme shown in Figure 13. By using this sequence of drainage and imbibition steps, we are able to simulate enhanced oil recovery, using injection of gas to mobilize oil remaining in the reservoir at the limit of imbibition.

a)

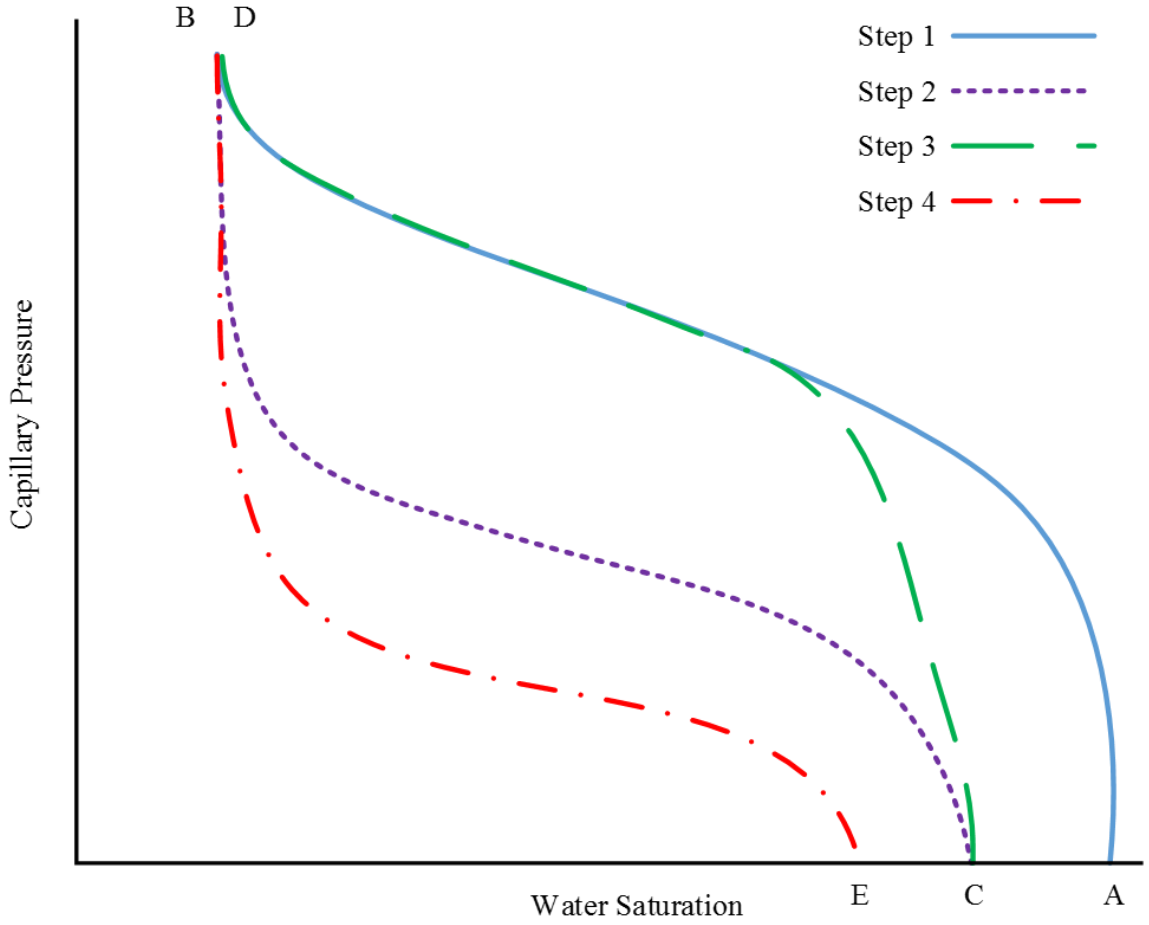

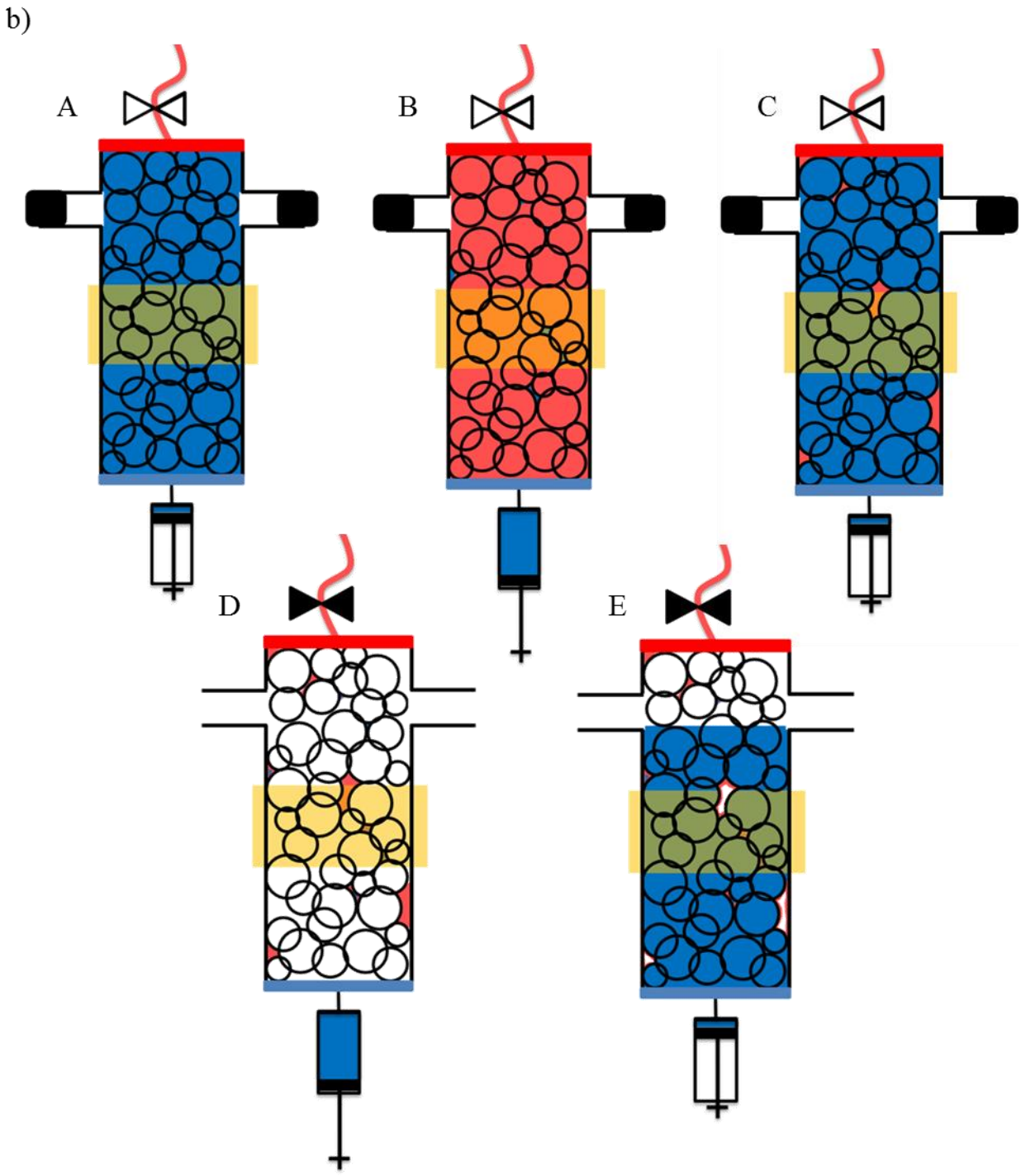

Figure 13: a) Pc- S curve of proposed experiment b) Example fluid distributions in the column corresponding to the proposed Pc-S curve

We begin with the glass bead column fully saturated with water (A). Step one in Figure 13 is drainage of the water from the column as oil is brought into the system. Drainage continues until the irreducible water saturation is reached in the column (B). This saturation can be identified by a spike in the pressure data. Once irreducible water saturation is reached, step two begins with water being imbibed into the system forcing oil out the top of the column. This process is stopped at a pressure drop indicating that the system has reached residual oil saturation (C), or the limit of imbibition. The water saturation cannot return to the initial 100% saturation because during the imbibition process some oil is left in the column, trapped or in films. The first two steps were performed to create some baseline two-phase flow data and prep the system for controlled three-phase displacement. In the third step, the third phase, air, is introduced into the system. A second drainage is performed with air vents opened on the side of the column about two thirds of the way up, seen in Figure 12a. During the second drainage the valve to the oil reservoir is closed, so no additional oil can enter the system. As drainage proceeds air enters the column until irreducible water saturation is reached (D). Then the fourth and final step of the experiment is initiated, a three-phase imbibition process. Water is pumped into the column and every phase can exit the column via the air vents on the sides creating a system of three-phase flow with each phase being mobile, ending at (E).

4.5 X-ray Settings

To achieve sufficient contrast between the fluid phases the monochromator is angled to produce x-rays with an energy level slightly above the iodine edge. The camera is set up to image at the middle of the column, and is positioned as close to the column as possible to achieve a high resolution. The dimensions of the resulting images are 1920x1920x1200 voxels, and require about 15-30 minutes to acquire depending on the exposure time. The imaging parameters used are in Table 5.

Table 5: Imaging Parameters

X-Ray Settings	Water-Wet System	Fractionally-Wet System
Energy	33.319 kev	33.269 kev
Exposure Time	1 s	1.5 s
Resolution	3.18 μm/pixel	3.79 μm/pixel

4.6 Image Processing

The images produced are greyscale images as seen in Figure 14.

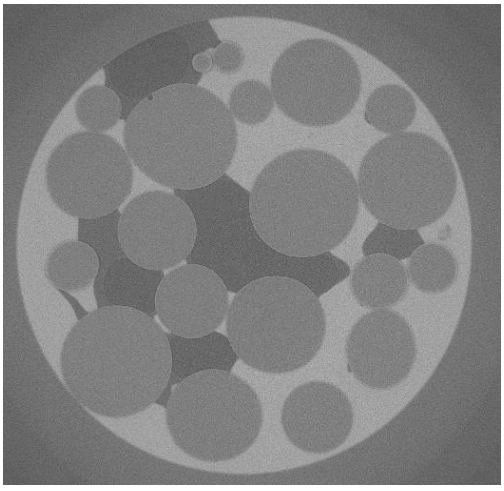

Figure 14: Greyscale image in 16-bit

During image processing the image is considered to be a four-phase image consisting of beads, air, water, and oil. Water is the brightest phase, then beads, oil, and air is the darkest. Each voxel has a value ranging between 0 and 65535 in the 16-bit image. The first goal of image processing is to designate every voxel with a label of 1 to 4, with each phase belonging to a separate class. Each experimental run required different image processing steps and parameters and the details are found in Appendix A.2.

4.6.1 Registration

An image of the dry bead pack, before fluids are introduced, is acquired at the beginning of each experiment. This dry image is used to designate where the beads are located enabling them to be easily distinguished in the image. However, throughout the course of the experiment, the beads may move or the column alignment might change. This causes a mismatch between the dry image and the points of interest (bead locations during fluid flow). To align the images a registration was performed using Elastix (Klein et al., 2010; Shamonin et al., 2014), via translation in all three directions as well as rotation. Post registration of the dry image can be used for accurate separation of the beads from the remaining fluid phases. To register an image on Elastix it must first be converted to 8bit, reducing the range of greyscale values to 0-255 shown in Figure 15.

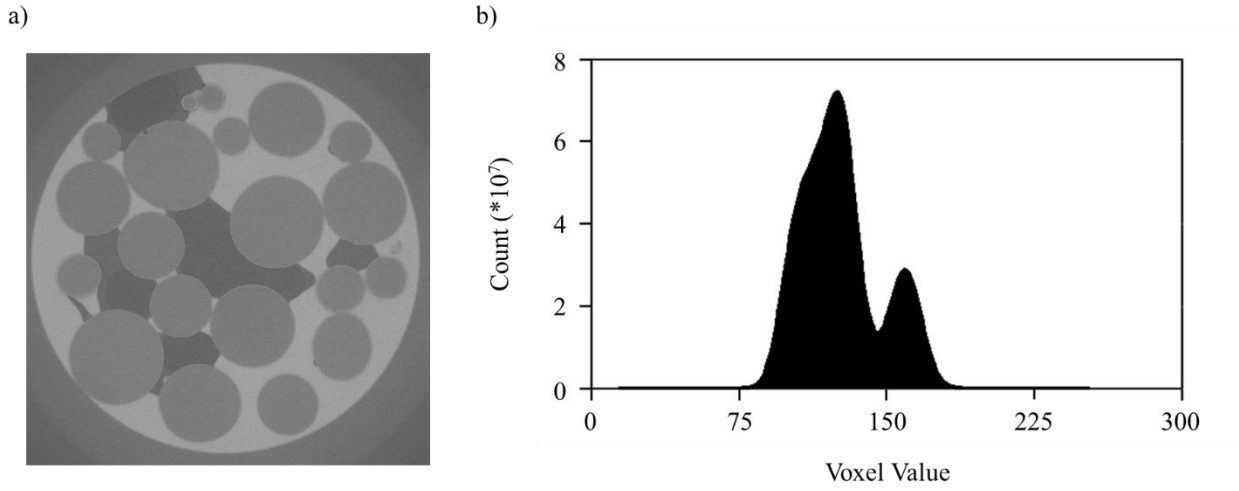

Figure 15: a) 8-bit Greyscale Image b) Unprocessed 8-bit histogram

4.6.2 Enhance Contrast

The 8-bit images do not have as high a contrast, as can be seen by the lack of distinct peaks in the histogram, Figure 15b. ImageJ was used to enhance the contrast between the phases by

stretching the histogram (Schneider et al., 2012). A designated 0.3%, of the greyscale values on the edge of the histogram were removed and the histogram is stretched to fill the full range, 0-255. Figure 16 shows the result of the enhance contrast step.

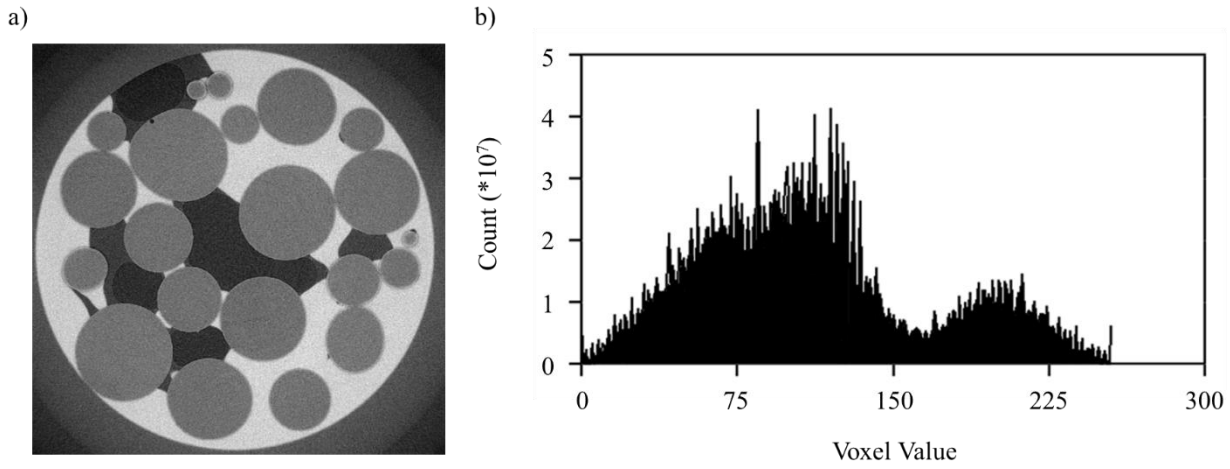

Figure 16: a) Enhance Contrast Image and b) Enhance Contrast Histogram

4.6.3 Smoothing

Image noise was removed using the Non-Local Means (NLM) filter on Avizo Fire®. The average value of all of the voxels in the image is determined and the result is weighted based on how similar the average value is to the target voxel. This filtering method reduces the amount of blurring at the edge of the phases as compared to other local filtering methods. The NLM filter results in an image that has very little noise and distinct peaks between the phases, Figure 17.

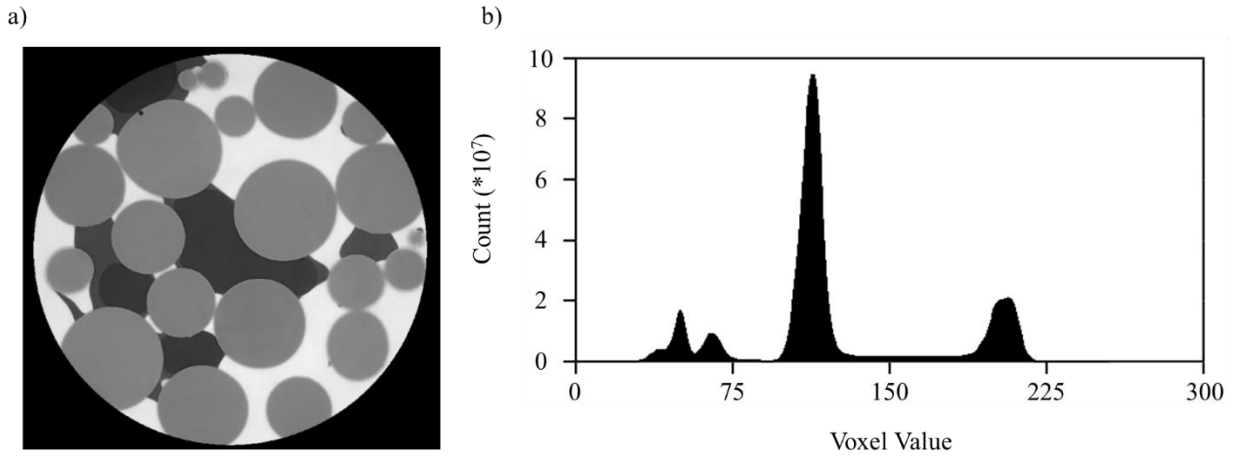

Figure 17: a) NLM Filtered Image and b) NLM Filtered Histogram

4.6.4 Thresholding

The image processing library Quantim4 was used to threshold and segment the images (http://www.quantim4.ufz.de). The threshold values were determined five different ways; maximum variance (Otsu, 1979), minimum error (Kittler & Illingworth, 1986), maximum entropy (Kapur et al., 1984), fuzzy c-means (Ridler & Calvard, 1978), and shape (Tsai, 1995). The average value from these methods was used in the subsequent Markov Random Field (MRF) segmentation; the threshold values used were also manually confirmed for each image as shown in Figure 18. The voxels shown in red in the image are those that fall within the red rectangle on the histogram.

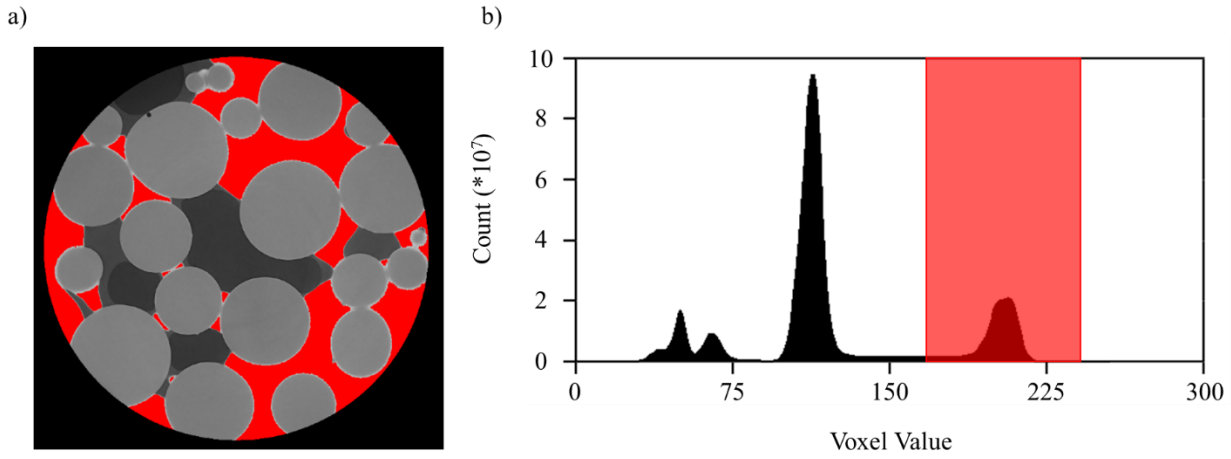

Figure 18: a) Image with threshold values for water b) Histogram depicting threshold values

4.6.5 Segmentation

Two different segmentation methods were used, Markov Random Field (MRF) and watershed (Kulkarni et al., 2012). The MRF method preserves films and oil layers better than the watershed method (Schluter et. al, 2014), so watershed was typically used to segment two-phase data and MRF was used to segment three-phase data. The MRF method did not provide a perfect segmentation, so each image was manually verified and a few voxel designations were altered to ensure proper labeling of each phase. An example of a final segmented image can be seen in Figure 19.

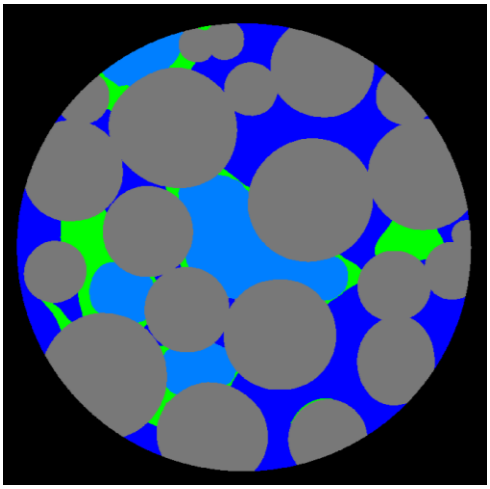

Figure 19: Segmented image: Beads (grey), Water (dark blue), Oil (green), Air (light blue)

4.7 Image Analysis

Once the images were segmented, they were further analyzed to generate quantitative measurements with respect to saturation, interfacial area, and capillary pressure (via curvatures).

4.7.1 Surface Generation

The example images shown in the image processing section are slices in the x-y plane of the three-dimensional image shown in Figure 20.

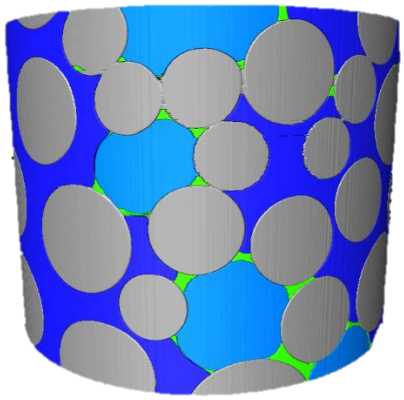

Figure 20: Three-dimensional segmented image

Each image is a set of surfaces representing the three different phases, which can be individually manipulated. The surfaces are generated via the marching cube algorithm (Lorensen & Cline, 1987), which locates the interface and creates a triangular mesh approximating a smooth surface. The surface generation function on Avizo Fire® allows for different smoothing settings, type and extent. We used constrained smoothing, which does not allow any labels to be altered, yet generates realistic surfaces. An increased smoothing extent only results in a smoother surface to a certain degree. An analysis of different smoothing extent values was performed, Figure 21, and the smoothing value was chosen based on a visual inspection of the surfaces. The result of smoothing extent used in each experiment are found in Appendix A.2.

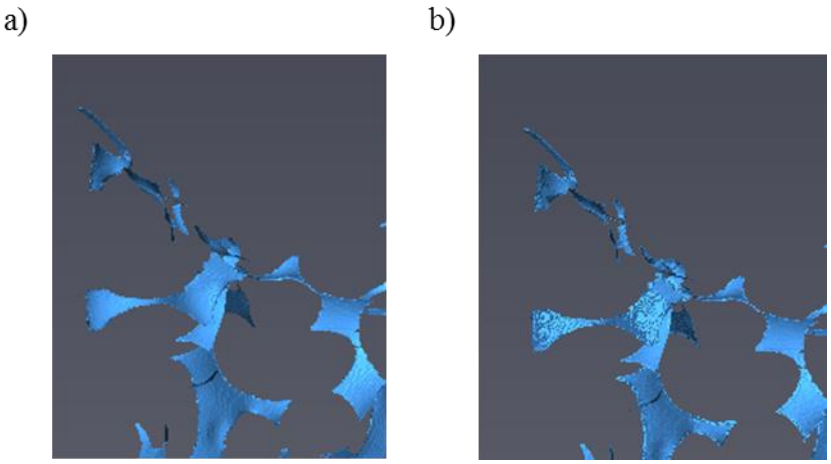

Figure 21: Smoothing Extent Images a) smoothing extent 3 b) smoothing extent 9

4.7.2 Saturation/Interfacial Area Measurement

Figure 22 shows the individual air, water and oil phase surfaces.

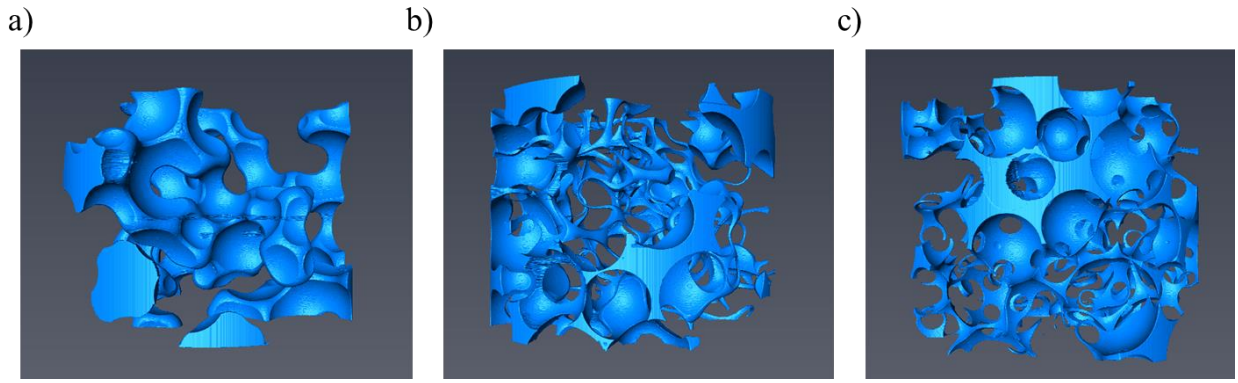

Figure 22: a)Air surface, b)Water Surface, c) Oil Surface

The number of voxels that make up each phase is recorded, and the saturation is found by dividing by the total number of fluid voxels.

Additionally, surfaces can be generated at the intersection between two different phase classes. Figure 23 depicts the fluid-fluid interfaces for each fluid pair.

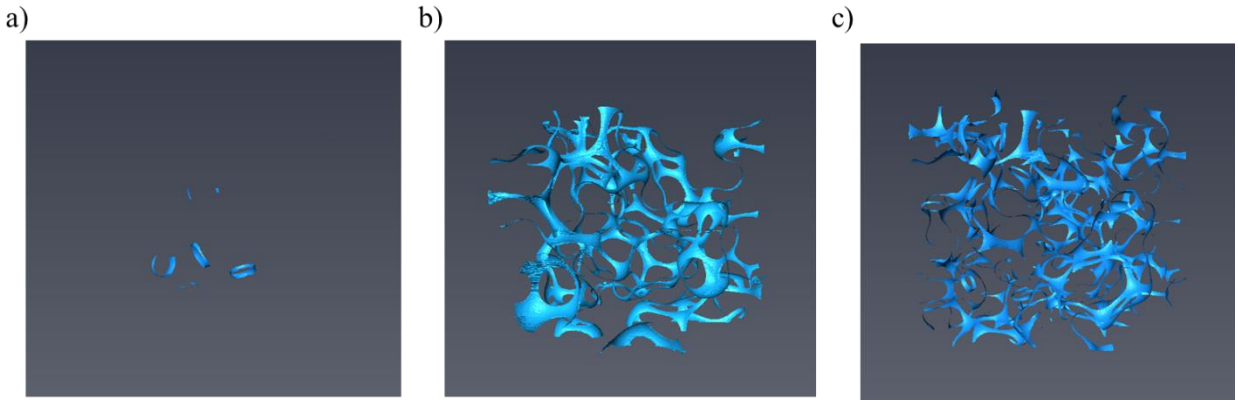

Figure 23: a) Air-Water Interface b) Air-Oil Interface c) Oil-Water Interface

The interfacial area is determined by summing the area of each triangle of the mesh on the generated interfacial surface. Note that very little air-water interfacial area is present in our data due to the presence of oil films between the air and water phases.

4.7.3 Connected and Disconnected Phases

Separating the connected and disconnected phases is an important step in determining the bulk phase curvatures. When fluids are trapped in the system, they maintain the pressure that they are at when they are disconnected from the bulk phase (Li et al., 2018). Since water enters the field of view from the bottom of the image for the water phase to be connected, it must be touching the bottom slice. This is done with a marker; it finds all of the voxels segmented into the water phase on the first slice and marks all water voxels that can be found connected to this slice. The same is done with the air and oil phases, except the marker is connected to the top slice of the image. The resulting image, Figure 24, consists of seven phases; beads (grey), connected water (dark blue), disconnected water (red), connected oil (green), disconnected oil (yellow), connected air (light blue), and disconnected air (orange).

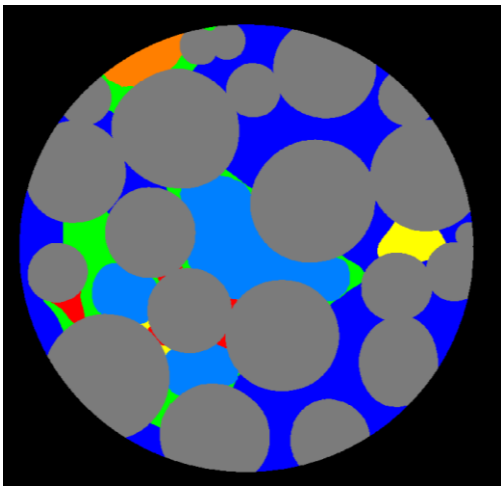

Figure 24: Segmented image separating connected and disconnected phases

Surfaces must be generated for the interfaces between each connected phase as well. The surfaces of the connected phases can be seen in Figure 25.

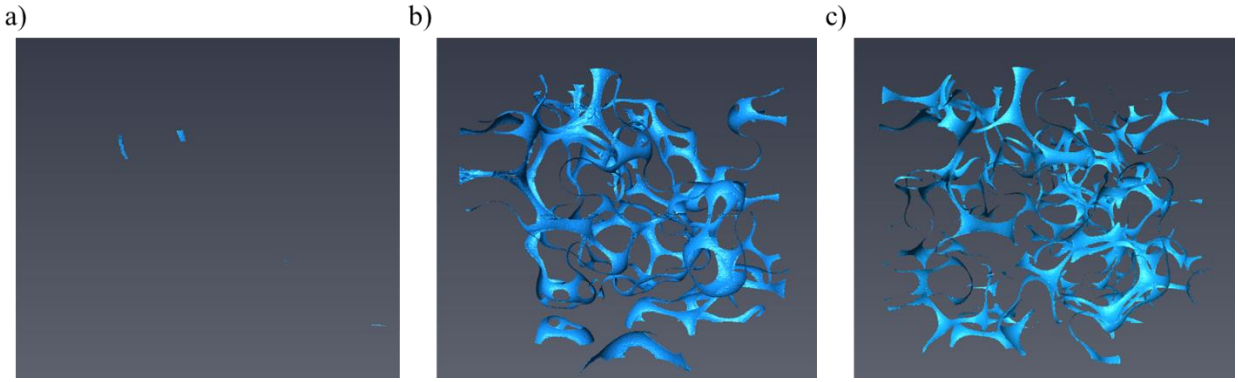

Figure 25: Connected phase surfaces: a) Air-Water b) Air-Oil c) Oil-Water

4.7.4 Curvature Measurement

To determine capillary pressure using the Young Laplace equation, Equation 9, the curvature of the fluid-fluid interface must be measured. Curvature is the degree to which the surface deviates from a flat plane. The Avizo Fire® mean curvature module is used to perform the measurement on the surfaces. At each triangle on the surface the two principal radii of curvature are determined and the mean curvature of the triangle is calculated via Equation 13 (Klingenberg, 1978).

$$H_i = \frac{1}{2}(\kappa_1 + \kappa_2) \qquad \text{Equation 13}$$

Where H is the mean curvature, and κ_i is a principal radius curvature of the surface of the triangle. The average curvature for all triangles is used as the mean curvature in the Young Laplace equation. Figure 26 shows the connected surfaces with the curvature values color mapped on them.

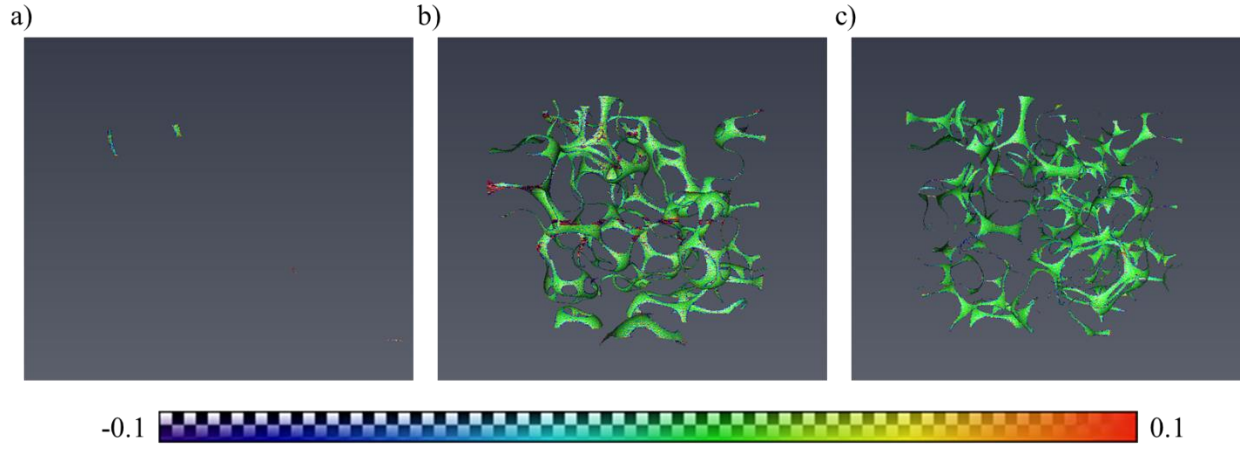

Figure 26: Connected Surface curvatures a) Air-Water b) Air-Oil c) Oil-Water

An accurate curvature based measurement of the air-water capillary pressure cannot be determined due to the limited connected air-water interfacial surfaces, so the air-water capillary pressure-saturation-interfacial area relationship will not be pursued in this study.

Due to the segmentation, the curvature values that are close to the solid bead surface are not as accurate as the curvatures far away from the beads. To account for this, the average curvatures are weighted based on their distance to a solid surface, Equation 14 (Li et al., 2018).

$$H_{DW} = \frac{\sum_i^N H_i D_i}{\sum_i^N D_i} \qquad \text{Equation 14}$$

Where D is the distance of each triangle, i, from the edge of the surface.

To reduce the effect of the edges on the curvature value even farther the surfaces are also clipped. The distance of each triangle to the edge of the surface is measured, and those triangles that fall within 20% of the maximum distance from the edge are removed from the distance weighted curvature average (Li et al., 2018).

From the curvature images, it is obvious that there are some small errors in the segmentation. The rough sections, where the color is red or purple, of the surface make up the extremes of the curvature values presented. A test was performed to determine what percent of the total histogram values would need to be removed to eliminate these values. To remove these sections only 0.028%-2.9% of the curvature values calculated across the image would be eliminated. These outliers make up a very small portion of the overall curvature values used when calculating the mean curvature, and were determined to be negligible.

During the two-phase portion of the experiment, a pressure transducer was used to measure the overall oil-water capillary pressure of the system. The measurements from the transducer were compared to the pressure values obtained via the Young Laplace equation to validate the use of curvature based capillary measurements, Figure 27.

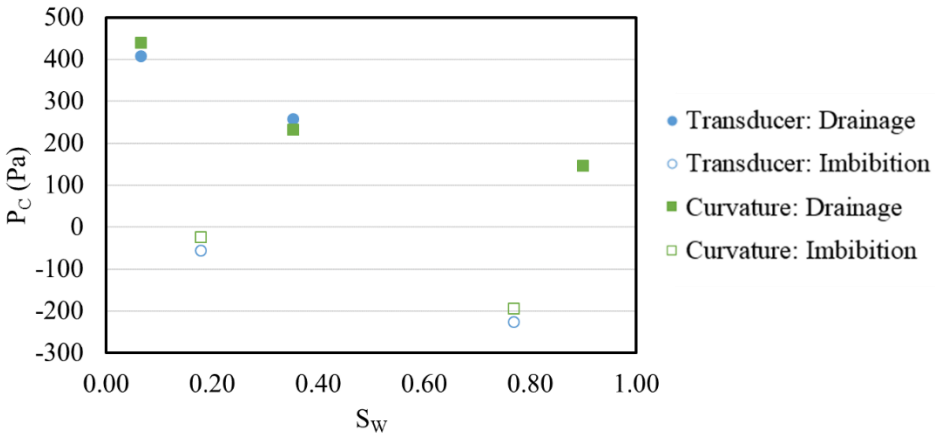

Figure 27: Comparison of transducer based pressure values and curvature based pressure values for water-wet system two-phase capillary pressure-saturation plot from run 3

The pressure data measured from the transducers matches well with the pressures derived from the curvatures, verifying the curvature measurement technique for our data.

5 Results

5.1 Wettability Alteration

In our three-phase water-wet system, three different experimental runs were combined to form one data set. However, in the capillary pressure-saturation relationship for the oil-water fluid pair, the third run does not seem to match well with the others, Figure 28.

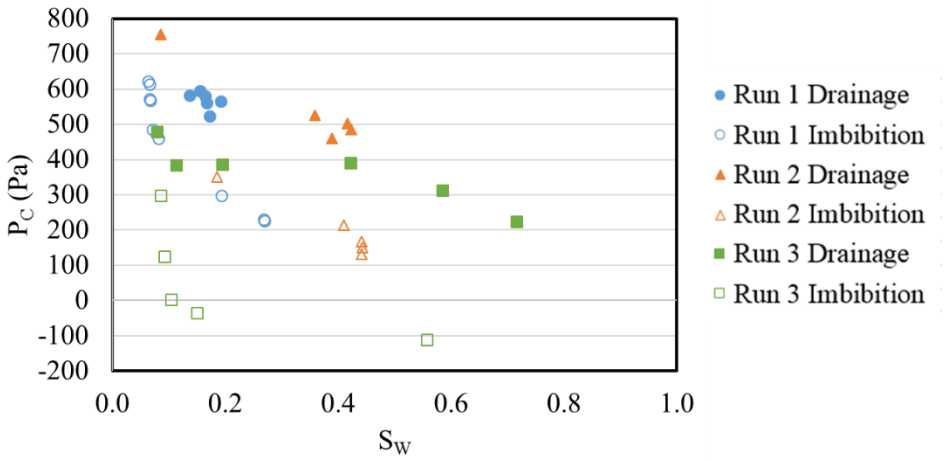

Figure 28: Three-phase water-wet system, oil-water fluid pair, capillary pressure-saturation relationship depicting wettability alteration

We suspect that the lowering of the capillary pressure for run 3 is due to wettability alteration of the bead pack caused by prolonged x-ray exposure of beads in contact with the oil phase, as described by Brown et al., 2014. The wettability alteration has the potential to affect the results by causing the water-wet data to trend towards more oil-wet behavior.

5.2 Comparison to Other Data Sets

To better understand our data, a comparison was made to other available data sets and the experimental characteristics for each of these data sets can be found in Table 6. For each experiment, the same distribution of glass beads was used as in our water-wet bead pack. In systems with interface relaxation flow was halted before each image was captured allowing the

fluid interfaces to relax into a quasi-equilibrium state, in systems without interface relaxation images were captured without stopping flow.

Table 6: Data set characteristics

Source	Fluid System	Oil Type	Spreading	Interface Relaxation	Three-Phase Invading Fluid	Flow Rate
Fractionally-wet System	Air-Oil-Water	decane	Non-spreading	Yes	Air	0.5 mL/h
Water-wet System	Air-Oil-Water	decane	Non-spreading	Yes	Air	0.5 mL/h
Wildenschild & Brown, 2012	Air-Oil-Water	Soltrol220	Spreading	Yes	Oil	0.5 mL/h
Schlüter et al., 2017	Oil-Water	n-dodecane	n/a	No	n/a	0.02 mL/h
Porter et al., 2010	Oil-Water	Soltrol220	n/a	Yes	n/a	0.6 mL/h
Wildenschild, 2009	Air-Water	n/a	n/a	Yes	n/a	6 mL/h
Culligan, 2004	Air-Water	n/a	n/a	Yes	n/a	0.25 mL/h
Meisenheimer & Wildenschild, in prep Transient	Air-Water	n/a	n/a	No	n/a	0.2 mL/h
Meisenheimer & Wildenschild, in prep Quasi-static	Air-Water	n/a	n/a	Yes	n/a	0.2 mL/h

In the Young Laplace equation, Equation 9, capillary pressure is dependent on interfacial tension. To compare data sets of different oil-water fluid pairs, the capillary pressures were scaled by a ratio of the interfacial tensions.

5.2.1 Two-Phase Oil-Water System

First comparing our data to Schlüter et al., 2017 two-phase oil-water data, Figure 29.

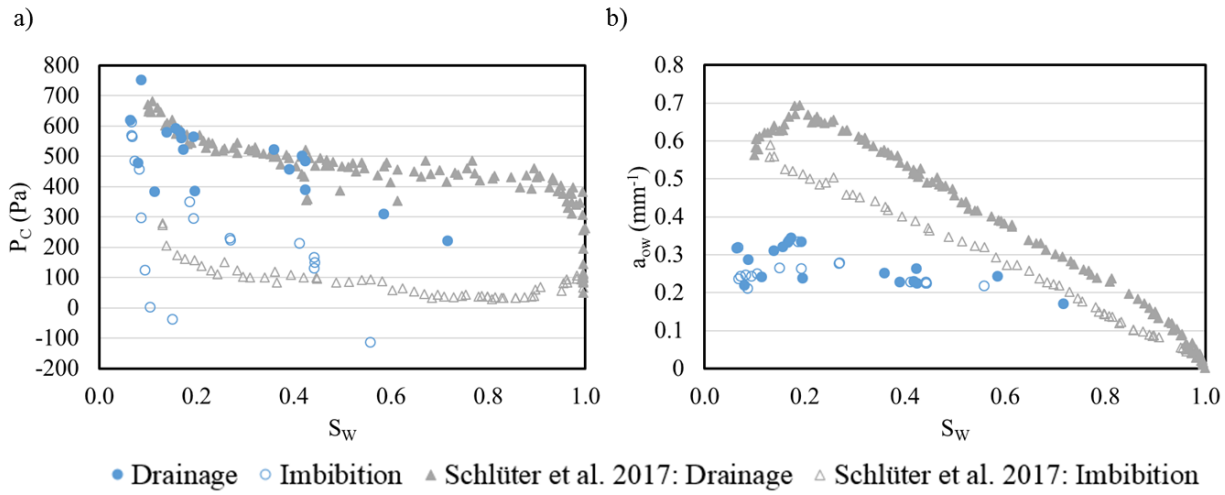

Figure 29: Comparison of water-wet oil-water fluid pair to Schlüter et al., 2017 a) Capillary pressure-saturation curve b) Interfacial area-saturation curve

Schlüter et al., 2017 data was collected with a very low flowrate allowing for the assumption that the system was always at a quasi-equilibrium state. By allowing for relaxation of the interfaces our three-phase experiments also achieved a quasi-equilibrium at each imaged saturation. The scaled capillary pressure-saturation curves, Figure 29a, show a strong match between the data collected by Schlüter et al., 2017 and our data, both validating our data's capillary pressure values and confirming the idea that interface relaxation does not affect capillary pressure of the system. The few data points that fall far below Schlüter et al., 2017 data are those suspected to have wettability alteration.

The interfacial area, however, is greatly affected by interface relaxation. The relaxation time allows for a rearrangement of the interfaces as they approach an equilibrium state. As the capillary pressure increases, or water saturation decreases, the effect of relaxation on the interfacial area also increases. This is most likely due to a greater departure from equilibrium as

pressures increase causing the amount of relaxation required to reach equilibrium to increase as well.

5.2.2 Three-Phase Oil-Water Spreading System

When comparing to Wildenschild & Brown, 2012 three-phase data, Appendix A.3, both the spreading characteristics of the oil and a different invading fluid must be taken into account. Figure 30 shows Wildenschild & Brown, 2012 data compared to our three-phase data for the oil-water fluid pair.

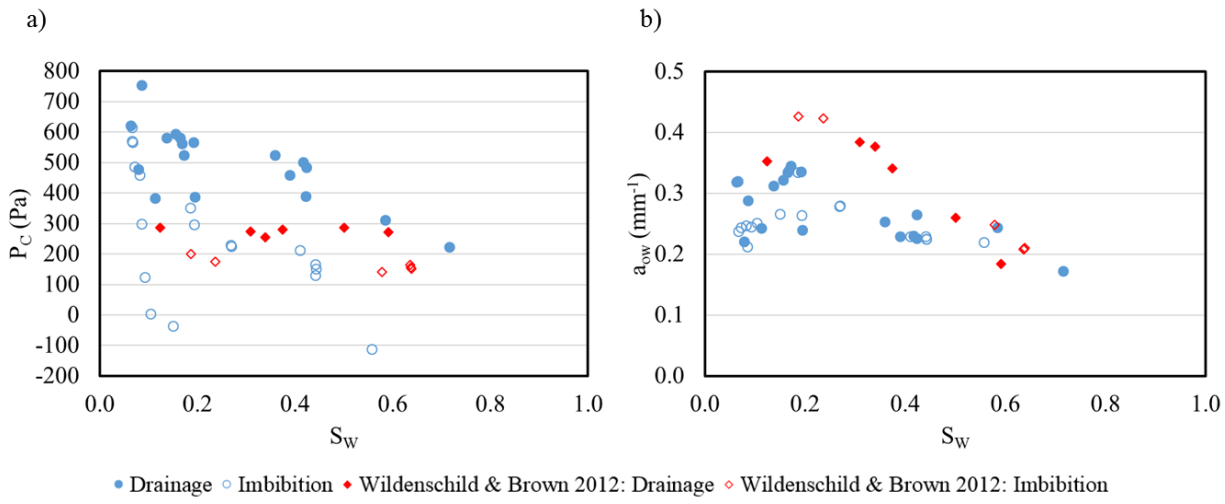

Figure 30: Comparison of water-wet oil-water fluid pair to Wildenschild & Brown, 2012 a) Capillary Pressure-Saturation curve b) Interfacial area-saturation plot

The differences in both capillary pressure and interfacial area appear as expected for a comparison between a spreading and a non-spreading system.

The interfacial areas for the spreading system are larger than those for the non-spreading system (Schaefer et al., 2000). The oil layers that form in a spreading system are stable and can be thinner than the layers formed in a non-spreading system. The non-spreading system layers are only due to the wettability affects, oil being the intermediate-wetting phase, and so they are

formed only by the displacement of the oil phase by the air phase as opposed to a molecular spreading between the fluids.

The capillary pressure-saturation plot also fits the expected trends for a spreading versus a non-spreading oil. The entry capillary pressure between the two systems is consistent, the slope, however, is drastically different (Mani & Mohanty, 1997). Non-spreading oils have unstable layers that at a threshold thickness become weak and break to form blobs. In order to move these blobs, a higher oil-water capillary pressure is needed, rather than to move oil in the hydraulically connected thin films of the spreading oil, at low water saturations. Additionally, it is expected that there will be more residual oil left in the system for the non-spreading oil due to increased trapping (Kalaydjian, 1992). The limit of imbibition for the non-spreading phase is approximately 55% water saturation, whereas for the spreading system it is approximately 65% water saturation. While the remaining saturation is a combination of oil and gas, it can be assumed that with a lower water saturation at the limit of imbibition there is more residual oil in the system. Recall that wettability alteration is the cause of the deviation of some of our results from the expected trends for a non-spreading water-wet system.

The systems compare as expected for a spreading and a non-spreading three-phase flow system, it is assumed that the differences observed are due to the spreading characteristics and not the effect of the differences in invading fluid, but this cannot be confirmed based on the available data.

5.3 Evaluation of Hysteresis

5.3.1 Interfacial Area-Saturation

From Figure 29b the magnitude of the hysteresis for the two-phase interfacial area-saturation relationship is greater than the magnitude of the hysteresis for the three-phase data. In fact, for the three-phase data it appears as if there is no hysteresis in the interfacial area-saturation relationship for the oil-water fluid pair. The extent and direction of the hysteresis was quantified via the hysteresis index (Zuecco et al., 2016) for all the data sets used for comparison. The two variables, water saturation and interfacial area, were first normalized. The normalized drainage and imbibition data for each data set was then plotted separately and a second-order

polynomial trendline was fitted. To remove outliers from the fit, a root mean square error (RMSE) value was calculated for each normalized data point to the fit. If the error was greater than 20% that data point was removed when generating the trendline used in the hysteresis index calculation. Also, since Wildenschild & Brown, 2012 data did not have any points at high water saturation an additional point was added at a water saturation of 100% and an interfacial area of 0 mm^{-1} to ensure a realistic fit for high water saturations.

The trendlines were then integrated and computed as in Equation 15.

$$A_{D[i,j]} = \int_i^j a_D(S_w)dS_w \qquad A_{I[i,j]} = \int_i^j a_I(S_w)dS_w \qquad \text{Equation 15}$$

Where the interval [i,j] used was 0.1, over the range of 0 to 1. The integrals were then subtracted at each interval, Equation 16.

$$\Delta A_{[i,j]} = A_{D[i,j]} - A_{I[i,j]} \qquad \text{Equation 16}$$

The hysteresis index, h, is then the sum of all ΔA, Equation 17.

$$h = \sum \Delta A_{[ij]} \qquad \text{Equation 17}$$

As the magnitude of the hysteresis index approaches 0 the extent of hysteresis in the system is reduced. The sign of h is also important, positive denotes a loop with drainage having the higher interfacial areas, and negative denotes a loop with imbibition having the higher interfacial areas. The magnitude and direction of the hysteresis index is presented in Figure 31.

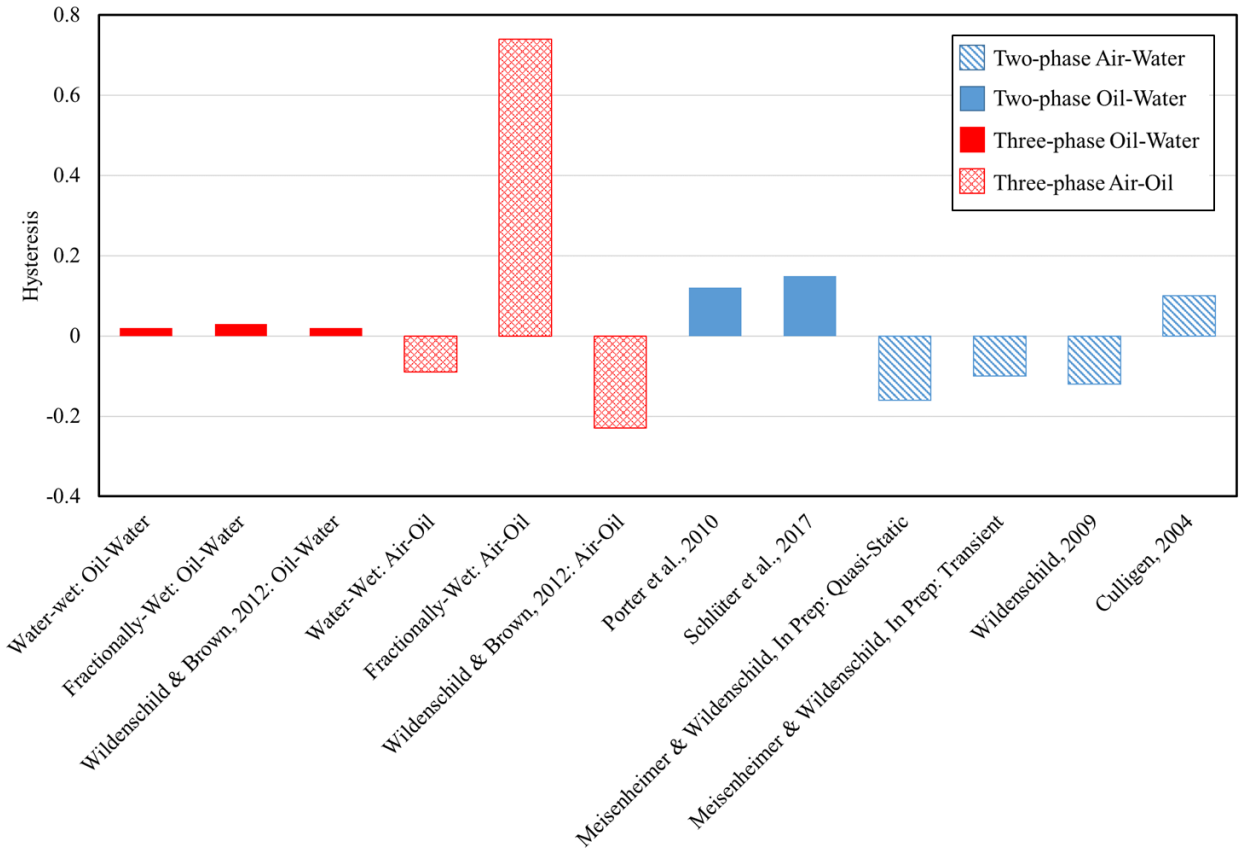

Figure 31: Extent of hysteresis in interfacial area-saturation relationship

The water-wet three-phase data we collected is a compilation of three different experimental trials. Figure 32 depicts the interfacial area-saturation relationship for the oil-water fluid pair.

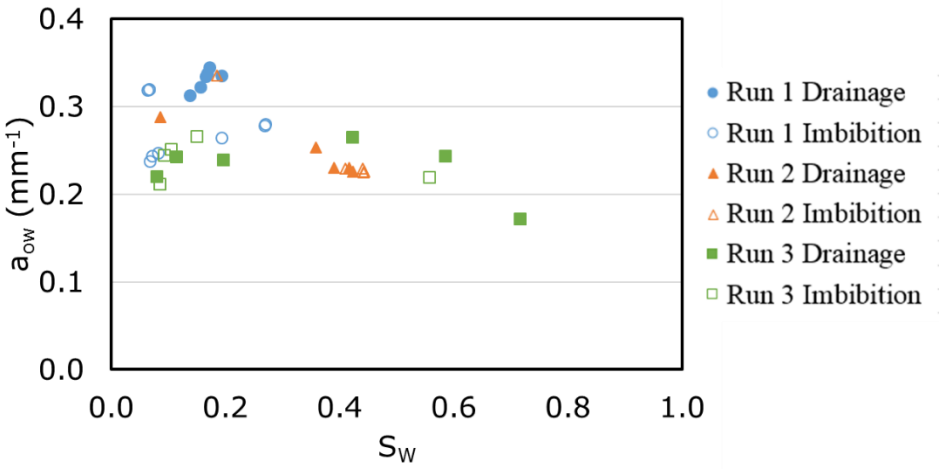

Figure 32: Water-wet three-phase data interfacial area-saturation relationship for oil-water fluid pair

We suspect the images that were collected for the first run did not have sufficient interface relaxation to reach a quasi-equilibrium state. The unrelaxed interfacial areas were significantly higher than the interfacial areas at similar saturations for the other runs, and so when included the fit for the water-wet data was not an accurate representation of the results. Therefore, the interfacial area data from the first run was removed for the extent of hysteresis calculations for both fluid pairs of the water-wet three-phase data set.

There is no noticeable difference in the amount of hysteresis between those data sets with and without interface relaxation, as well as between different two-phase fluid pairs. However, there is a significant decrease in the magnitude of hysteresis for three-phase oil-water data compared to any of the other data sets tested. The magnitude of the hysteresis index is negligible and so three-phase oil-water interfacial area data can be assumed to be non-hysteretic. The three-phase air-oil interfacial area-saturation relationship data is more hysteretic. The spreading, Wildenschild & Brown, 2012, and the fractionally-wet air-oil systems have significantly higher magnitude of the hysteresis index.

Additionally, the hysteresis index calculations can be used to determine the shape of the hysteresis loop by comparing the minimum and maximum $\Delta A_{[i,j]}$. If the minimum and the

maximum value have opposite signs then the loop takes on an eight-shape (Zuecco et al., 2016). All of the three-phase data, for both fluid pairs, has this eight-shape effect, depicted in Figure 33.

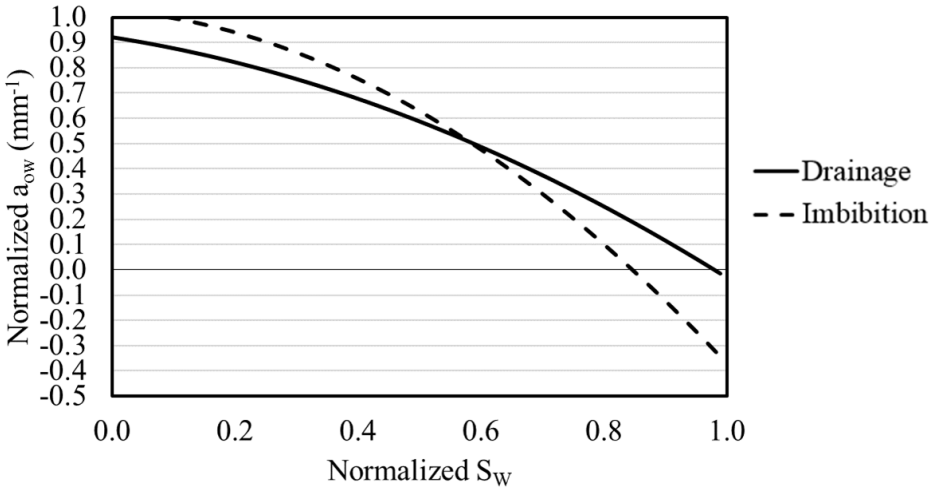

Figure 33: Eight-shape hysteresis loop, depicted via the second-order polynomial trendlines from Wildenschild & Brown, 2012 oil-water data

For the two-phase data, Porter et al., 2010 is the only data set that has the eight shape, and the cross-over occurs at very high water saturations where the interfacial area measurements are not as accurate, suggesting that it is the trendline fit causing the eight-shape, and not a characteristic of the data set.

5.3.2 Capillary Pressure-Saturation-Interfacial Area Relationships

The capillary pressure-saturation-interfacial area surfaces were modeled using a bi-quadratic equation, Equation 18, similar to Porter et al., 2009.

$$a_{nw}(P_c, S_w) = A * {P_c}^2 + B * P_c + C * P_C * S_w + D * S_w + E * {S_w}^2 + F \quad \text{Equation 18}$$

Where A, B, C, D, E, F are best-fit parameters. The parameters used for each surface generated are shown in Appendix A.4. The model used was unable to find best fit parameters when capillary pressure values were negative, so for the fractionally-wet bead pack oil-water fluid pair

model 400 Pa was added to all of the capillary pressure values before determining the best fit parameters. The root mean square error (RMSE) for the drainage and imbibition surfaces of the fractionally-wet bead pack are undefined because there are so few data points that the accuracy of each surface is unknown. Figure 34 depicts the unique surfaces for oil-water and air-oil fluid pairs. Recall, that there was an insufficient amount of interfacial area present to establish data for the air-water interfaces.

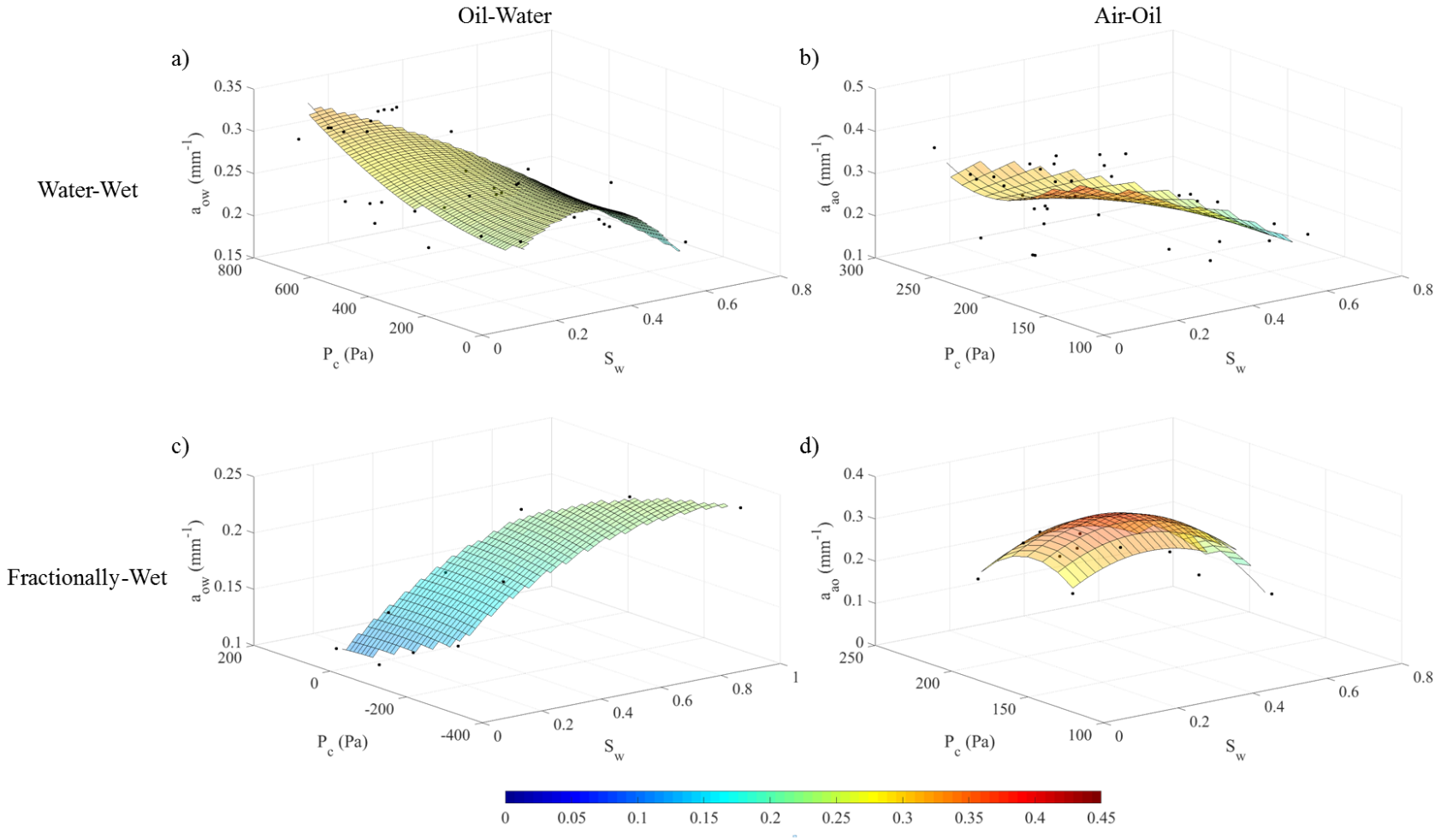

Figure 34: Capillary Pressure-saturation-interfacial area surfaces a) water-wet bead pack oil-water surface b) water-wet bead pack air-oil surface c) fractionally-wet bead pack oil-water surface d) fractionally-wet bead pack air-oil surface

To determine an acceptable amount of error to consider surfaces similar a test was performed on the water-wet bead pack surface model for both fluid pairs. When generating the surfaces for the water-wet bead pack, data from all three runs was combined. The RMSE and the mean absolute error (MAE) were found for the unique surface compared to the individual surfaces generated from each run. Since these runs all had the same experimental characteristics, the maximum error generated between individual run surfaces and the unique surface model will be the threshold for determining if surfaces are similar. The error thresholds used can be found in Table 7.

Table 7: Error threshold determination

Fluid Pair	RMSE	MAE
Oil-Water	0.030	0.027
Air-Oil	0.069	0.058

To test Hassanizadeh & Gray, 1990 theory regarding the uniqueness of the capillary pressure-saturation-interfacial area relationship for three-phase flow systems the RMSE and MAE were calculated between the drainage and imbibition surfaces, as well as each of them against the unique surface generated for the system. The error values are presented in Table 8.

Table 8: Error between surfaces

Bead Pack	Fluid Pair	Surfaces	RSME	MAE
Water-Wet Beads	Oil-Water	Drainage/Imbibition	0.024	0.028
		Unique/Drainage	0.023	0.021
		Unique/Imbibition	0.024	0.021
	Air-Oil	Drainage/Imbibition	0.11	0.10
		Unique/Drainage	0.034	0.030
		Unique/Imbibition	0.057	0.052
Fractionally-Wet Beads	Oil-Water	Drainage/Imbibition	n/a	n/a
		Unique/Drainage	0.008	0.007
		Unique/Imbibition	0.021	0.017
	Air-Oil	Drainage/Imbibition	n/a	n/a
		Unique/Drainage	0.022	0.030
		Unique/Imbibition	0.014	0.017

5.3.2.1 Water-Wet System

For the water-wet bead pack oil-water, fluid pair the error in all three surface pairs is negligible, meaning that the capillary pressure-saturation-interfacial area surface eliminates the hysteresis in this system. Figure 35 depicts the water-wet bead pack oil-water fluid pair drainage and imbibition surfaces.

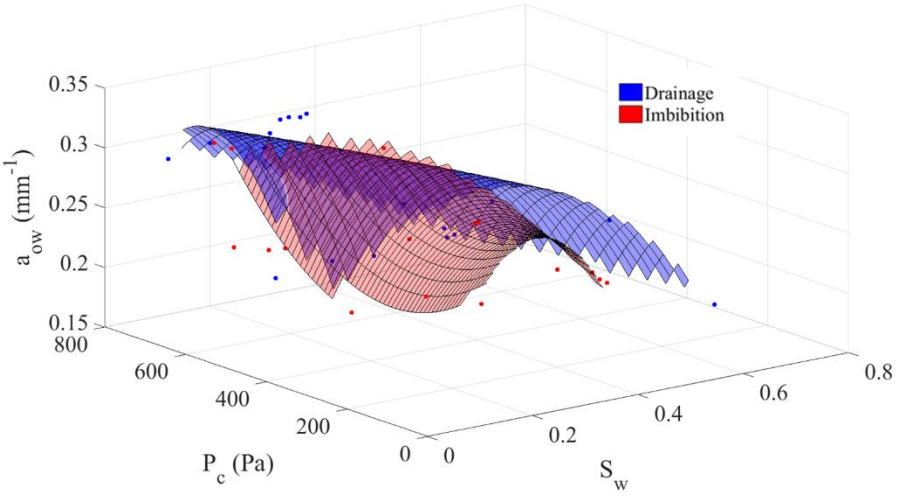

Figure 35: Capillary pressure-saturation-interfacial area surfaces of drainage and imbibition for water-wet bead pack oil-water fluid pair

For the water-wet bead pack air-oil fluid pair the error in the drainage and imbibition surface is not negligible, and there is a significant difference between these two surfaces, Figure 36.

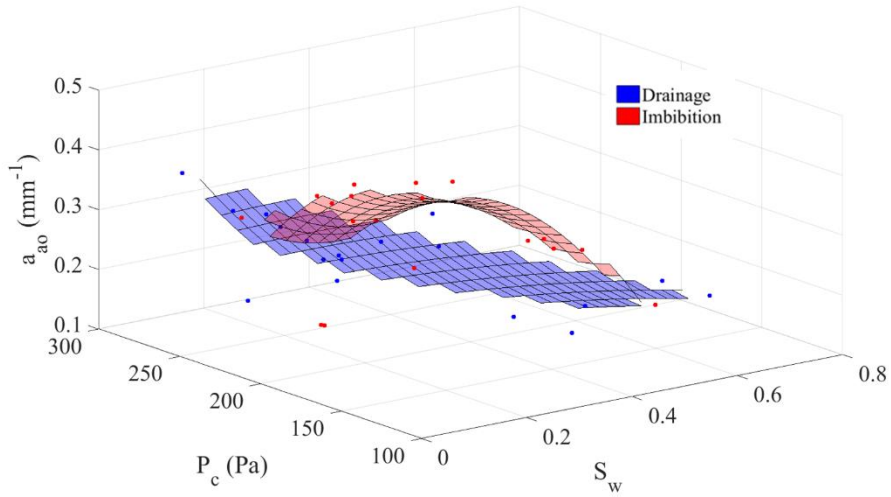

Figure 36: Capillary pressure-saturation-interfacial area surfaces of drainage and imbibition for water-wet bead pack air-oil fluid pair

This supports the findings based on the hysteresis index presented earlier, where a higher degree of hysteresis was observed for air-oil data sets. The difference between the drainage and unique surface is considered negligible, but the difference between the imbibition surface and the unique surface is not. We cannot eliminate the possibility that hysteresis exists in the capillary pressure-saturation-interfacial area surface for the air-oil fluid pair in a water-wet bead pack, however, since the hysteresis is eliminated in one fluid pair, oil-water, we suspect that energetically hysteresis must also be eliminated in the other fluid pairs. Therefore, we assume that the variation is due more to scatter then to the presence of hysteresis.

5.2.3.2 Fractionally-Wet System

Again, due to the limited number of data points, there is no error information for the drainage/imbibition surface comparison for the fractionally-wet beads, because these surfaces do not overlap on the capillary pressure-saturation plane, Figure 37.

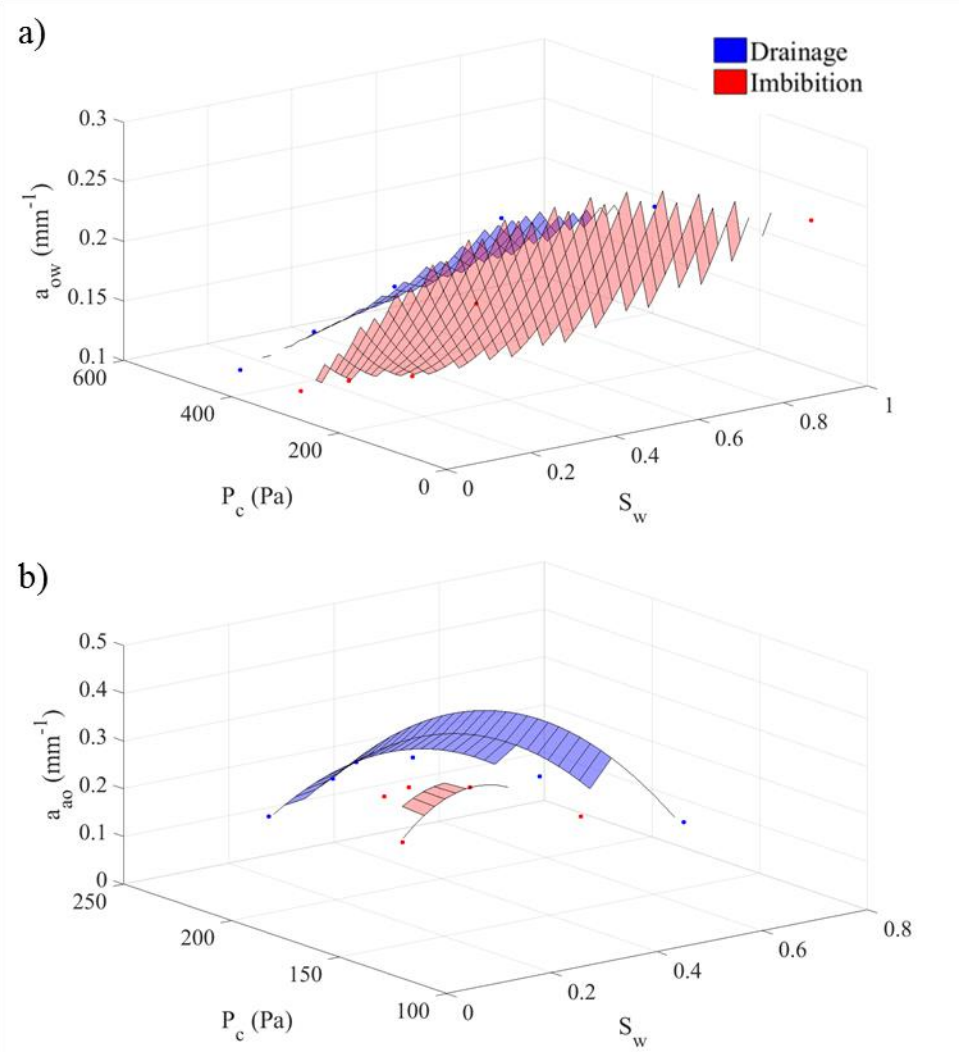

Figure 37: Fractionally-wet capillary pressure-saturation-interfacial area surface shown in the capillary pressure-saturation plane for a) oil-water and b) air-oil

However, we were able to compare the drainage surface to the unique surface and the imbibition surface to the unique surface. The variance between the drainage and the imbibition surfaces with the unique surface is within acceptable limits, so both can be accurately represented by the unique surface. The elimination of hysteresis from the surface, however, cannot be completely determined without more data to allow for an overlap between the drainage and imbibition surfaces.

5.4 Comparison of Water-Wet System to Fractionally-Wet System

To analyze the effects of wettability on the three-phase capillary pressure-saturation-interfacial area relationships the porous media systems of the different tests must be similar. For the water-wet bead pack the porosity ranged from 30-35%. The fractionally-wet bead pack had a porosity of 30%. Additionally, in the range of imaging, the oil-wet beads made up 63% of the bead surface area. Recall, that we are now only discussing effects of wettability as both data sets are non-spreading and the experimental conditions were otherwise identical.

5.4.1 Oil-Water Fluid Pair

Wettability has a significant effect on the capillary pressure-saturation-interfacial area relationship for the oil-water fluid pair, Figure 38.

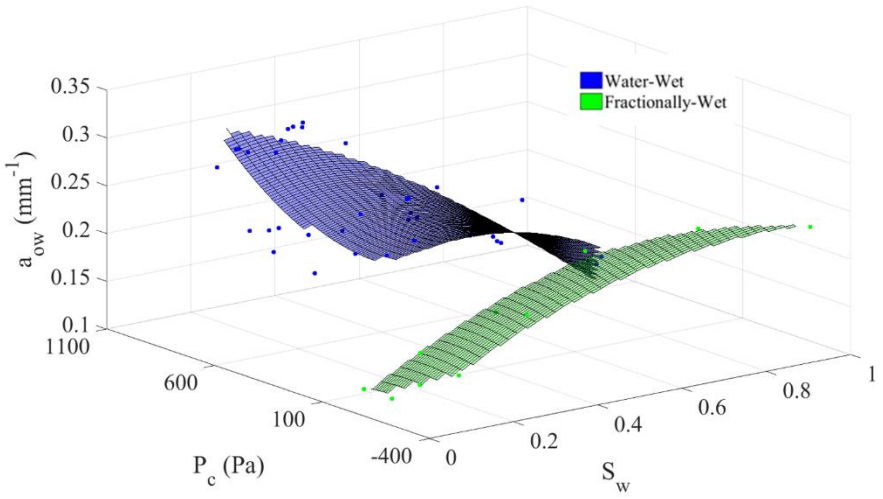

Figure 38: Comparison of water-wet bead pack and fractionally-wet bead pack capillary pressure-saturation-interfacial area surface for the oil-water fluid pair

The two surfaces do not overlap and have distinctly different shapes. This is expected due to the changing of the wetting order between water and oil within different pores in the system. The effects of wettability can be seen more clearly in the two-dimensional capillary pressure-saturation and interfacial area-saturation plots, Figure 39.

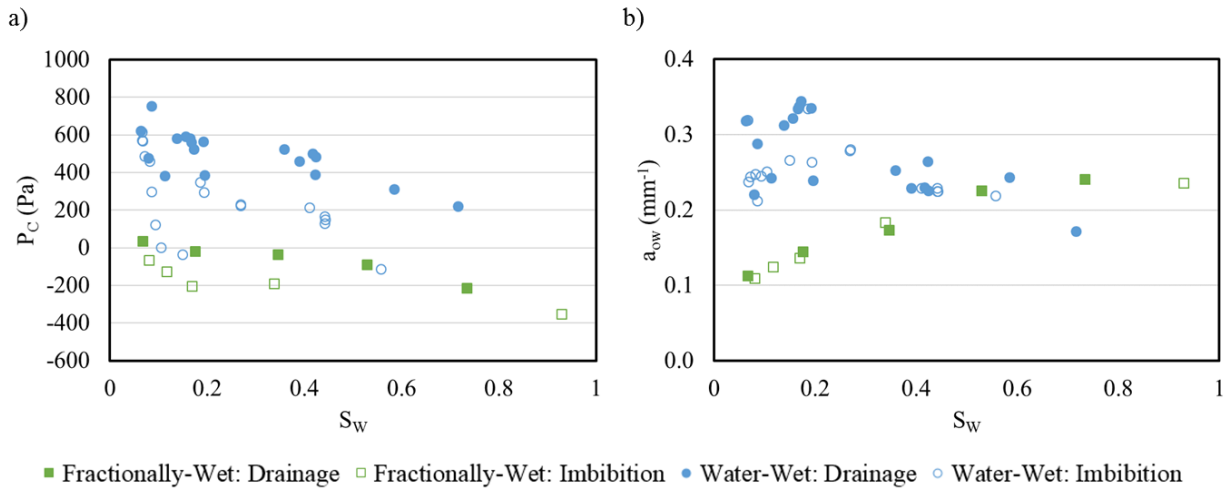

Figure 39: Oil-Water comparison of water-wet bead pack to fractionally-wet bead pack of a) capillary pressure-saturation and b) interfacial area-saturation

As expected, the fractionally-wet bead pack has significantly lower capillary pressures than the water-wet bead pack for the same water saturations. The curvature is always determined through the water phase, and so in an oil-wet pore, the curvature value would be negative, resulting in a negative pressure. Thus, in a bead pack with pores of different wettabilities, some capillary pressures are negative and some are positive, sometimes along a single interface, illustrated in Figure 40, resulting in a lower overall mean curvature value across the system, and therefore, a lower capillary pressure.

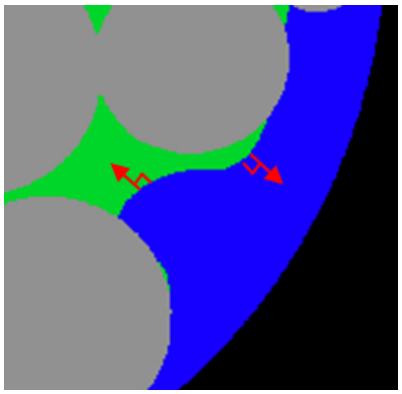

Figure 40: Image from fractionally-wet bead pack depicting both a positive (water-wet) and negative (oil-wet) curvature. Beads (grey), Oil, (green), Water (dark blue)

Additionally, the hysteresis in the fractionally-wet capillary pressure-saturation relationship is less pronounced than in the water-wet system. Due to the wettability variability across the pores there is a mixture of wetting and drying in each drainage or imbibition step.

The interfacial area data shows drastic differences between the water-wet bead pack and the fractionally-wet bead pack. While the maximum interfacial area value generated in both systems is similar, the slope of the interfacial area change with water saturation is opposite. As water saturation decreases in the water-wet bead pack, water tends to become trapped in the corners of pores, as well as form small hydraulically connected films along the beads increasing the surface area of the water, which creates an interface with the intermediate-wetting oil film. These water films allow for an increase in surface area as the water saturation decreases. Conversely, for the fractionally-wet bead pack the water does not become trapped in the corners of pores, and therefore at low saturations there is very little surface area to create an interface resulting in a decrease in interfacial area as the water saturation decreases. However, when looking at the wetting phase saturation, as opposed to only the water saturation, the bead packs follow the same trend, as the wetting phase saturation decreases the interfacial area increases.

5.4.2 Air-Oil Fluid Pair

The air-oil fluid pair capillary pressure and interfacial area do not seem to be affected by wettability. An RMSE of 0.044 mm^{-1} and MAE of 0.038 mm^{-1} was found when the fractionally-wet surface and the water-wet surface was compared, Figure 41.

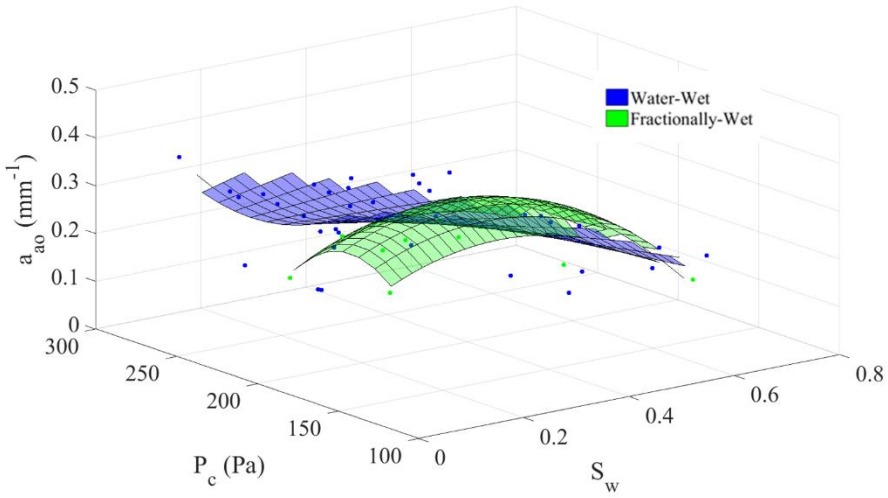

Figure 41: Comparison of water-wet bead pack and fractionally-wet bead pack capillary pressure-saturation-interfacial area surface fort the air-oil fluid pair

These error values are less than the determined threshold, and so these surfaces can be considered similar. Figure 42 depicts the capillary pressure-saturation and interfacial area-saturation two-dimensional plots.

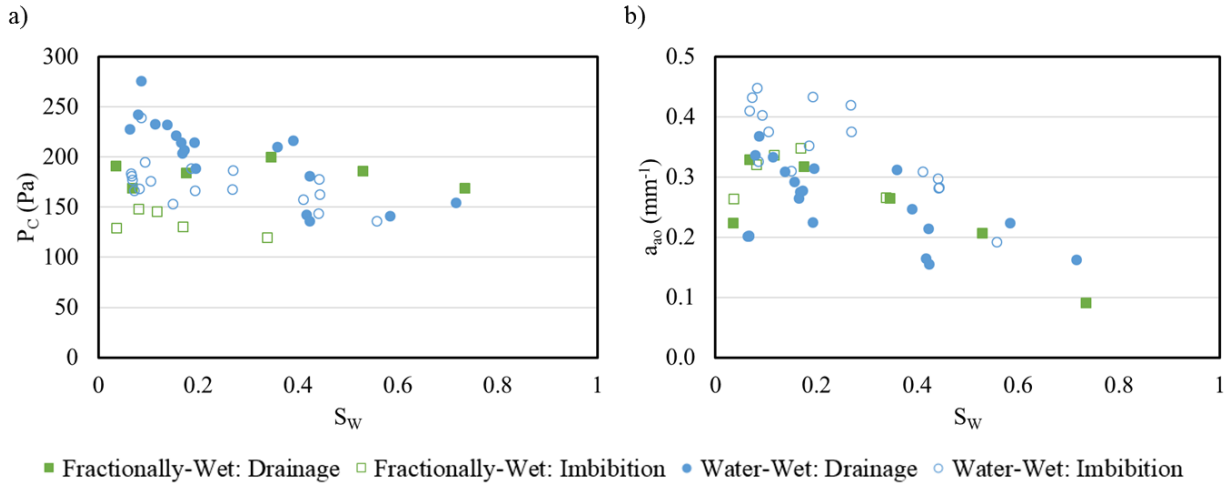

Figure 42: Air-Oil comparison of water-wet bead pack to fractionally-wet bead pack of a) capillary pressure-saturation and b) interfacial area-saturation

From these two-dimensional plots, Figure 42, it can be more clearly seen that there is very little variation among the two wettabilities. The air-oil interfacial area is not dependent on the wettability of the bead pack, and there is only a slight variation of the capillary pressure-saturation relationship among the wettabilities. The fractionally-wet capillary pressure data is slightly lower than that of the water-wet bead pack for low water saturations, however this is most likely due to experimental variation rather than wettability effects. These results indicate that the air-oil fluid pair is not affected by the wettability of the system, since the wetting order of these two fluids is not altered.

6 Conclusion

In this study, we examined the relationship between capillary pressure, saturation, and interfacial area for a three-phase flow system. Using x-ray microtomography we were able to capture high-resolution three-dimensional images of the flow system, from which the saturation, interfacial area, and capillary pressure were determined. The main research findings are summarized here:

6.1 Hysteretic Effects

- For oil-water fluid pair two-dimensional interfacial area-saturation relationship, hysteresis is negligible in a three-phase flow system.
- For the water-wet system oil-water fluid pair, the three-dimensional capillary pressure-saturation-interfacial area relationship eliminates hysteresis.
- For the water-wet system air-oil fluid pair there is a significant difference between the drainage and imbibition three-dimensional capillary pressure-saturation-interfacial area relationships.
- For both fluid pairs in the fractionally-wet system it is unlikely that there is hysteresis in the three-dimensional capillary pressure-saturation-interfacial area relationship, but this cannot be confirmed due to limited data.

6.2 Wettability Effects

- For the oil-water fluid pair there is significant difference in the three-dimensional capillary pressure-saturation-interfacial area relationship as wettability is altered from water-wet to a fractionally-wet system with 63% of the surface area oil-wet.
- For the oil-water fluid pair, as water saturation increases, the interfacial area decreases for a water-wet system, but increases for a fractionally-wet system.
- For the air-oil fluid pair the three-dimensional capillary pressure-saturation-interfacial area relationship is not affected by wettability in a three-phase flow system.

6.3 Implications and Future Study

These results are applicable to three-phase non-spreading flow systems with invading air. However, more study on the capillary pressure-saturation-interfacial area relationship needs to be completed to verify these results. For the fractionally-wet system, only one experimental trial was performed, and so there is not enough data to fully describe and understand the system. Additionally the experimental trials for the water-wet system had both wettability alteration, in run 3, and only limited interface relaxation, in run 1. Further testing of this system is needed to ensure that those variations do not significantly influence the overall relationship.

An area for future study could be on the relationship between each fluid pair interfacial areas. Understanding of how the energetics of the different fluid pair systems interact could help further characterize the three-phase system with a relationship that combines all three fluid phase interactions.

The relationships presented here can be used to generate a more sophisticated model to predict three-phase fluid movements in a porous medium.

Bibliography

Agrawal, D., & Menon, V. (1992). Surface tension and evaporation: An emperical relation for water. *Physical Review A*, *46*(4), 2166–2169.

Al-futaisi, A., & Patzek, T. W. (2003). Impact of wettability alteration on two-phase flow characteristics of sandstones : A quasi-static description. *Water Resources Research*, *39*(2), 1–13. https://doi.org/10.1029/2002WR001366

Al-Raoush, R. I., & Willson, C. S. (2005). A pore-scale investigation of a multiphase porous media system. *Journal of Contaminant Hydrology*, *77*(1-2), 67–89. https://doi.org/10.1016/j.jconhyd.2004.12.001

Armstrong, R. T., Porter, M. L., & Wildenschild, D. (2012). Linking pore-scale interfacial curvature to column-scale capillary pressure. *Advances in Water Resources*, *46*, 55–62. https://doi.org/10.1016/j.advwatres.2012.05.009

Armstrong, R. T., & Wildenschild, D. (2012). Microbial Enhanced Oil Recovery in Fractional-Wet Systems : A Pore-Scale Investigation. *Transport in Porous Media*, *92*, 819–835. https://doi.org/10.1007/s11242-011-9934-3

Bentsen, R. G., & Trivedi, J. J. (2012). Modified Transport Equations For the Three-Phase Flow of Immiscible, Incompressible Fluids Through Water-Wet Porous Media. *Journal of Porous Media*, *15*(2), 123–136.

Blunt, M. J. (2001). Flow in porous media - Pore-network models and multiphase flow. *Current Opinion in Colloid and Interface Science*, *6*(3), 197–207. https://doi.org/10.1016/S1359-0294(01)00084-X

Blunt, M. J. (2017). *Multiphase Flow in Permeable Media: A Pore-Scale Perspective*. Cambridge: University Printing House. https://doi.org/10.1017/9781316145098

Blunt, M. J., Bijeljic, B., Dong, H., Gharbi, O., Iglauer, S., Mostaghimi, P., … Pentland, C. (2013). Pore-scale imaging and modelling. *Advances in Water Resources*, *51*, 197–216.

Bradford, S. a, & Leij, F. J. (1996). Predicting two- and three-fluid capillary pressure-saturation relationships of porous media with fractional wettability. *Water Resources*, *32*(2), 251–259.

Brown, K., Schluter, S., Sheppard, A., & Wildenschild, D. (2014). On the challenges of measuring interfacial characteristics of three-phase fluid flow with x-ray microtomography. *Journal of Microscopy*, *253*(3), 171–182. https://doi.org/10.1111/jmi.12106

Brusseau, M. L., Peng, S., Schnaar, G., & Costanza-Robinson, M. S. (2006). Relationships among air-water interfacial area, capillary pressure, and water saturation for a sandy porous medium. *Water Resources Research*, *42*(3), 1–5. https://doi.org/10.1029/2005WR004058

Burton, C. S., Mayo, J. R., & Cunningham, I. A. (2015). Theoretical and experimental comparison of image signal and noise for dual-energy subtraction angiography and conventional x-ray angiography. In *Progress in Biomedical Optics and Imaging - Proceedings of SPIE*. https://doi.org/10.1117/12.2082724

Caubit, C., Bertin, H., & Hamon, G. (2004). Three-Phase Flow in Porous Media : Wettability Effect on Residual Saturations During Gravity Drainage and Tertiary Waterflood. *Society of Petroleum Engineers*.

Chen, D., Pyrak-Nolte, L. J., Griffin, J., & Giordano, N. J. (2007). Measurement of interfacial area per volume for drainage and imbibition. *Water Resources Research*, *43*(12), 1–6. https://doi.org/10.1029/2007WR006021

Culligan, K. A., Wildenschild, D., Christensen, B. S. B., Gray, W. G., Rivers, M. L., & Tompson, A. F. B. (2004). Interfacial area measurements for unsaturated flow through a porous medium. *Water Resources Research*, *40*, 1–12. https://doi.org/10.1029/2004WR003278

Diamantopoulos, E., Durner, W., & Harter, T. (2016). Prediction of capillary air-liquid interfacial area vs. saturation function from relationship between capillary pressure and water saturation. *Advances in Water Resources*, *97*, 219–223. https://doi.org/10.1016/j.advwatres.2016.09.012

Fenwick, D. H., & Blunt, M. J. (1998). Three-dimensional modeling of three phase imbibition and drainage. *Advances in Water Resources*, *21*(2), 121–143. https://doi.org/10.1016/S0309-1708(96)00037-1

Ferrand, L. A., Milly, P. C. ., Pinder, G. F., & Turrin, R. P. (1990). A Comparison of Capillary Pressure-Saturation relations for Drainage in Two- and Three-Fluid Porous Media. *Advances in Water Resources*, *13*(2), 54–63.

Hassanizadeh, S. M., & Gray, W. G. (1990). Mechanics and thermodynamics of multiphase flow in porous media including interphase boundries. *Advances in Water Resources*, *13*(4), 169–186.

Hassanizadeh, S. M., & Gray, W. G. (1993). Thermodynamic basis of capillary pressure in porous media. *Water Resources Research*, *29*(10), 3389–3405. https://doi.org/10.1029/93WR01495

Held, R. J., & Celia, M. a. (2001). Modelling support of functional relationships between capillary pressure, saturation, interfacial area and common lines. *Advances in Water Resources*, *24*(3-4), 325–343. https://doi.org/10.1016/S0309-1708(00)00060-9

Helland, J. O., & Skjaeveland, S. M. (2006). Three-phase mixed-wet capillary pressure curves from a bundle of triangular tubes model. *Journal of Petroleum Science and Engineering*, *52*(1-4), 100–130. https://doi.org/10.1016/j.petrol.2006.03.018

Helland, J. O., & Skjaeveland, S. M. (2007). Relationship between capillary pressure, saturation, and interfacial area from a model of mixed-wet triangular tubes. *Water Resources Research*, *43*(12), 1–15. https://doi.org/10.1029/2006WR005698

Holm, R., van Dijke, M. I. J., & Geiger, S. (2010). Three-phase flow modelling using pore-scale capillary pressures and relative permeabilities for mixed-wet media at the continuum-scale. *Transport in Porous Media*, *81*(3), 423–442. https://doi.org/10.1007/s11242-009-9415-0

Holtzman, R., & Segre, E. (2015). Wettability Stabilizes Fluid Invasion into Porous Media via Nonlocal , Cooperative Pore Filling. *Physical Review Letters*, *115*(16). https://doi.org/10.1103/PhysRevLett.115.164501

Hughes, R. G., & Blunt, M. J. (2000). Pore Scale Modeling of Rate Effects in Imbibition. *Transport in Porous Media*, *40*, 295–322.

Hui, M.-H., & Blunt, M. J. (2000). Effects of wettability on three-phase flow in porous media. *The Journal of Physical Chemistry B*, *104*, 3833–3845. https://doi.org/10.1021/jp9933222

Humphry, K. J., Suijkerbuijk, B. M. J. M., van der Linde, H. A., Pieterse, S. G. J., & Masalmeh, S. K. (2014). Impact of Wettability on Residual Oil Saturation and Capillary Desaturation Curves. *Petrophysics*, *55*(4), 313–318.

Iassonov, P., & Tuller, M. (2010). Application of Segmentation for Correction of Intensity Bias in X-Ray Computed Tomography Images. *Vadose Zone Journal*, *9*(January), 187–191. https://doi.org/10.2136/vzj2009.0042

Joekar-Niasar, V., & Hassanizadeh, S. M. (2012). Uniqueness of Specific Interfacial Area-Capillary Pressure-Saturation Relationship Under Non-Equilibrium Conditions in Two-Phase Porous Media Flow. *Transport in Porous Media*, *94*(2), 465–486. https://doi.org/10.1007/s11242-012-9958-3

Kalaydjian, F. .-M. (1992). Performance and Analysis of Three-Phase Capillary Pressure Curves for Drainage and Imbibition in Porous Media. *SPE Annual Technical Conference and Exhibition*. https://doi.org/10.2118/24878-ms

Kantzas, a., Nikakhtar, B., & Pow, M. (1998). Principles of three phase capillary pressures. *Journal of Canadian Petroleum Technology*, *37*(7), 48–54. https://doi.org/10.2118/98-07-05

Kapur, J. N., Sahoo, P. K., & Wong, A. K. . (1984). A New Method for Gray-Level Picture Thresholding Using the Entropy of the Histogram. *Computer Vision, Graphics, and Image Processing*, *29*, 273–285.

Khishvand, M., Alizadeh, a. H., & Piri, M. (2016). In-situ characterization of wettability and pore-scale displacements during two- and three-phase flow in natural porous media. *Advances in Water Resources*, *97*, 279–298. https://doi.org/10.1016/j.advwatres.2016.10.009

Kittler, J., & Illingworth, J. (1986). Minimum Error Thresholding. *Pattern Recognition*, *19*(1), 41–47.

Klein, S., Staring, M., Murphy, K., Viergever, M. A., & Pluim, J. P. W. (2010). elastix : A Toolbox for Intensity-Based Medical Image Registration. *IEEE Transactions on Medical Imaging*, *29*(1), 196–205.

Kulkarni, R., Tuller, M., Fink, W., & Wildenschild, D. (2012). Three-Dimensional Multiphase Segmentation of X-Ray CT Data of Porous Materials Using a Bayesian Markov Random Field Framework. *Vadose Zone Journal*, *11*. https://doi.org/10.2136/vzj2011.0082

Lenhard, R. . (1992). Meausrement and modeling of three-phase saturation-pressure hysteresis. *Journal of Contaminant Hydrology*, *9*, 243–269.

Lenhard, R. ., & Parker, J. . (1987). Measurement and prediction of saturation-pressure relationships in three-phase porous media systems. *Journal of Contaminant Hydrology*, *1*(4), 407–424.

Lenormand, R., Touboul, E., & Zarcone, C. (1988). Numerical models and experiments on immiscible displacements in porous media. *Journal of Fluid Mechanics*, *189*, 165–187.

Li, T., Schlüter, S., Ines, M., & Wildenschild, D. (2018). An improved method for estimating capillary pressure from 3D microtomography images and its application to the study of disconnected nonwetting phase. *Advances in Water Resources*, *114*, 249–260. https://doi.org/10.1016/j.advwatres.2018.02.012

Lorensen, W. E., & Cline, H. E. (1987). Marching Cubes: A High Resloution 3D Surface Construction Algorithm. *Computer Graphics*, *21*(4), 163–169.

Mani, V., & Mohanty, K. (1997). Effect of the Spreading Coefficient on Three-Phase Flow in Porous Media. *Journal of Colloid and Interface Science*, *187*(1), 45–56. https://doi.org/10.1006/jcis.1996.4700

Mcgovern, M. E., Kallury, K. M. R., & Thompson, M. (1994). Role of Solvent on the Silanization of Glass with Octadecyltrichlorosilane. *Langmuir*, *10*(10), 3607–3614.

Mcketty, M. (1998). The AAPM/RSNA Physics Tutorial for Residnets X-ray Attenuation. *Imaging and Therapeutic Technology*, *18*(1), 151–163.

Meisenheimer, D., Wildenschild, D. (In Prep). Fast X-ray microtomography study of transient vs. quasi-static two-phase flow. *Water Resources Research*

Morrow, N. R. (1970). Physics and Thermodynamics of Capillary Action in Porous Media. *Industrial and Engineering Chemistry*, *62*(6), 32–56. https://doi.org/10.1021/ie50726a006

Otsu, N. (1979). A Threshold Selection Method from Gray-Level Histograms. *IEEE Transactions on Systems, Man, and Cybernetics*, *SMC-9*(1), 62–66.

Piri, M., & Blunt, M. J. (2004). Three-phase threshold capillary pressures in noncircular capillary tubes with different wettabilities including contact angle hysteresis. *Physical Review E - Statistical, Nonlinear, and Soft Matter Physics*, *70*(6 1), 1–17. https://doi.org/10.1103/PhysRevE.70.061603

Porter, M. L., Schaap, M. G., & Wildenschild, D. (2009). Lattice-Boltzmann simulations of the capillary pressure – saturation – interfacial area relationship for porous media. *Advances in Water Resources*, *32*(11), 1632–1640. https://doi.org/10.1016/j.advwatres.2009.08.009

Porter, M. L., Wildenschild, D., Grant, G., & Gerhard, J. I. (2010). Measurement and prediction of the relationship between capillary pressure, saturation, and interfacial area in a NAPL-water-glass bead system. *Water Resources Research*, *46*(8), 1–10. https://doi.org/10.1029/2009WR007786

Raeesi, B., & Piri, M. (2009). The effects of wettability and trapping on relationships between interfacial area, capillary pressure and saturation in porous media: A pore-scale network modeling approach. *Journal of Hydrology*, *376*(3-4), 337–352. https://doi.org/10.1016/j.jhydrol.2009.07.060

Reeves, P. C., & Celia, M. A. (1996). A functional relationship between capillary pressure , saturation , and interfacial area as revealed by a pore-scale network model. *Water Resources Research*, *32*(8), 2345–2358.

Ridler, T. W., & Calvard, S. (1978). Picture Thresholding Using an Iterative Selection Method. *IEEE Transactions on Systems, Man, and Cybernetics*, *SMC-8*(8), 630–632.

Rolo, L. I., Caco, A. I., Queimada, A. J., Marrucho, I. M., & Coutinho, J. A. . (2002). Surface Tension of Heptane, Decane, Hexadecane, Eicosane, and Some of Their Binary Mixtures. *Journal of Chemical Engineering*, *47*, 1442–1445.

Schaefer, C. E., Dicarlo, D. A., & Blunt, M. J. (2000). Determination of Water-Oil Interfacial Area during 3-Phase Gravity Drainage in Porous Media. *Journal of Colloid and Interface Science*, *221*, 308–312. https://doi.org/10.1006/jcis.1999.6604

Schlüter, S., Berg, S., Li, T., Vogel, H.-J., & Wildenschild, D. (2017). Time scales of relaxation dynamics during transient conditions in two-phase flow. *Water Resources*, *53*, 4709–4724. https://doi.org/10.1002/2016WR019815.Received

Schluter, S., Sheppard, A., Brown, K., & Wildenschild, D. (2014). Image processing of multiphase images obtained via X-ray microtomography: A review. *Water Resources Research*, 3615–3639. https://doi.org/10.1002/2014WR015256.Received

Schneider, C. A., Rasband, W. S., & Eliceiri, K. W. (2012). NIH Image to ImageJ : 25 years of image analysis. *Nature Methods*, *9*(7), 671–675. https://doi.org/10.1038/nmeth.2089

Seth, S., & Morrow, N. R. (2007). Efficiency of the Conversion of Work of Drainage to Surface Energy for Sandstone and Carbonate. *SPE Reservoir Evaluation and Engineering*, (August), 24–27.

Shamonin, D. P., Bron, E. E., Boudewijn, P., Lelieveldt, P., Smits, M., Klein, S., & Staring, M. (2014). Fast parallel image registration on CPU and GPU for diagnostic classification of Alzheimer ' s disease. *Frontiers in Neuroinformatics*, *7*(January), 1–15. https://doi.org/10.3389/fninf.2013.00050

Singh, K., Bijeljic, B., & Blunt, M. J. (2016). Imaging of Oil layers, curvature and contact angle in a mixed-wet and a water-wet carbonate rock. *Water Resources Research*, *52*(3), 1716–1728. https://doi.org/10.1002/2015WR018072.Received

Spiteri, E. J., Juanes, R., Blunt, M. J., & Orr, F. M. (2008). A New Model of Trapping and Relative Permeability Hysteresis for All Wettability Characteristics. *SPE Journal*, *13*(3), 277–288.

Tsai, D. (1995). A fast thresholding selection procedure for multimodal and unimodal histograms. *Pattern Recognition Letters*, *16*, 653–666.

Van Dijke, M. I. J., McDougall, S. R., & Sorbie, K. S. (2001). Three-phase capillary pressure and relative permeability relationships in mixed-wet systems. *Transport in Porous Media*, *44*(1), 1–32. https://doi.org/10.1023/A:1010773606657

Van Dijke, M. I. J., & Sorbie, K. S. (2002). Pore-scale network model for three-phase flow in mixed-wet porous media. *Physical Review E - Statistical, Nonlinear, and Soft Matter Physics*, *66*(4), 1–14. https://doi.org/10.1103/PhysRevE.66.046302

Van Dijke, M. I. J., & Sorbie, K. S. (2004). Consistency of three-phase capillary entry pressures and pore phase occupancies. *Developments in Water Science*, *55*(PART 1), 163–174. https://doi.org/10.1016/S0167-5648(04)80046-7

Van Dijke, M. I. J., Sorbie, K. S., Sohrabi, M., & Danesh, a. (2004). Three-Phase Flow WAG Processes in Mixed-Wet Porous Media: Pore-Scale Network Simulations and Comparison

With Water-Wet Micromodel Experiment. *SPE Journal*, *9*(1), 57–66. https://doi.org/10.2118/87822-PA

Vogel, H.-J. (n.d.). Quantim4. Helmhotz Center for Environmental Research. Retrieved from http://www.quantim4.ufz.de

Wildenschild, D. (2009). Experimental analysis of non-equlibrium processes for multiphase flow in porous media. 2009 SIAM Conference on Mathmatical and Computational Issues in the Geosciences, Leipzig, Germany, 15-18 June.

Wildenschild, D., Brown, K. (2012). Imaging and quantifying three-phase flow in porous media. Abstract H52C-05 presented at 2012 Fall Meeting, AGU, San Francisco, Calif., 3-7 Dec.

Wildenschild, D., Hopmans, J. W., Vaz, C. M. P., Rivers, M. L., Rikard, D., & Christensen, B. (2002). Using X-ray computed tomography in hydrology : systems , resolutions , and limitations. *Journal of Hydrology*, *267*, 285–297.

Wildenschild, D., & Sheppard, A. P. (2013). X-ray imaging and analysis techniques for quantifying pore-scale structure and processes in subsurface porous medium systems. *Advances in Water Resources*, *51*, 217–246. https://doi.org/10.1016/j.advwatres.2012.07.018

Wilhelm Klingenberg. (1978). *A Course in Differential Geometry*.

Zeppieri, S., Rodriguez, J., & Lopez de Ramos, A. (2001). Interfacial Tension of Alkane + Water Systems. *Journal of Chemical Engineering*, *46*(582), 1086–1088. https://doi.org/10.1021/je000245r

Zuecco, G., Penna, D., Borga, M., & Meerveld, H. J. Van. (2016). A versatile index to characterize hysteresis between hydrological variables at the runoff event timescale, *1466*(December 2015), 1449–1466. https://doi.org/10.1002/hyp.10681

APPENDICES

A.1 Remove Intensity Drift

In the greyscale image, the voxels in the center tend to be more intense, having a higher greyscale value, than the voxels on the edges of the image in the x-y direction. There can also be intensity drift variation in the z-direction, where average greyscale values for a phase can vary from the top to the bottom of the image. A smoothing function, Equation 19, is applied to the image to reduce the amount of variation in intensity over the image.

$$I(r) = a + b\cos\left(\frac{2\pi r}{R}\right) + c\exp\left(\frac{r}{R}\right) \qquad \text{Equation 19}$$

Where I is the intensity of each voxel and r is the radial position and R is the radius of the sample (Iassonov & Tuller, 2010). The intensity drift correction greatly reduces the unevenness in the greyscale values.

A.2 Image Processing Parameters

Table A.1: Image Processing Parameters

Trial	Intensity Drift (Direction)	Registration Parameters	Enhance Contrast Saturation	NLM filter Parameters	Segmentation Method	Surface Smoothing Extent	Curvature Absolute Value
Water-wet Run 1 two-phase	n/a	Resolutions: 5 Image sampler: Full	0.3	21-5-0.4	MRF	3	Yes
Water-wet Run 1 three-phase	Z direction	Resolutions: 5 Image sampler: Full	0.3	21-5-0.4	MRF	3	Yes
Water-wet Run 2 two-phase	n/a	Resolutions: 3 Image Sampler: Random	0.3	15-5-2	Watershed	5	No
Water-wet Run 2 three-phase	n/a	Resolutions: 3 Image Sampler: Random	0.3	15-5-2	MRF	5	No
Water-wet Run 3 two-phase	X-Y direction	Resolutions: 3 Image Sampler: Random	0.3	15-5-2	MRF/Watershed	5	No
Water-wet Run 3 three-phase	n/a	Resolutions: 3 Image Sampler: Random	0.3	15-5-2	MRF	5	No
Fractionally-wet three-phase	Z direction	Resolutions: 3 Image Sampler: Random	0.3	15-5-2	MRF	3	No

A.3 Wildenschild & Brown, 2012 Methods

A three-phase water-wet system was generated. Soda-lime glass beads were used to generate the bead pack, the size distribution is similar to the water-wet system in Table 2. The glass beads were placed in a 5.6 mm diameter borosilicate glass column, and sintered for 15 minutes at 760 °C, ensuring the beads would not move throughout the experiment. The fluids used in this system were air, water, and Soltrol220. Cesium was used as the contrast agent in the water phase, 1:6 ratio, and iodine was used as the contrast agent for the oil phase, 1:9 ratio. The interfacial tensions between the fluids are in Table A.2.

Table A.2: Fluid Pair Interfacial Tensions: Wildenschild & Brown, 2012

Fluid Pair	Interfacial Tension (dyne/cm)
Air/Water-cesium	71
Soltrol220-iodine/Water-cesium	37
Air/Soltrol220-iodine	25

Initially, water was pumped into bottom of the column at a flowrate of 0.5 mL/h trapping small air bubbles throughout the system until the water level reached the top of the column. The pore space was flushed with three pore volumes of water ensuring the remaining air was immobile. The top of the column was then connected to the oil reservoir. First, primary drainage, water was drained from the system while oil was pulled in from the top of the column until the system reached irreducible water saturation. Then, for primary imbibition, water was imbibed back into the system pushing the oil out the top of the column until the water reached the top of the column. Scanning drainage and imbibition curves were then created by draining and imbibing the water to points of mid-range water saturation.

X-ray microtomography images were captured at different saturation points along the aforementioned drainage and imbibition curves. Three images were captured, each at a different energy, for every data point. First above the cesium edge (36.1 keV), then above the iodine edge (33.3 keV), and finally below the iodine edge (33.1 keV). The resolution of the images was 9.24 μm/pixel.

A.4 Surface Best-Fit Parameters

Table A.3: Best-fit Parameters

Bead Pack	Fluid Pair	Surface	A	B	C	D	E	F	RMSE
Water-Wet Beads	Oil-Water	Unique	1.742e-07	2.396e-05	-2.345e-04	0.325	-0.511	0.209	0.035
		Drainage	-2.210e-06	0.003	-0.004	2.903	-2.006	-0.814	0.026
		Imbibition	7.511e-07	-3.937e-04	6.810e-04	0.937	-1.960	0.186	0.027
	Air-Oil	Unique	-2.016e-05	-0.010	0.007	-1.491	6.947e-04	1.482	0.072
		Drainage	8.460e-06	-0.003	6.798e-04	-0.109	-0.136	0.431	0.049
		Imbibition	1.606e-05	-0.007	0.004	0.122	-1.884	1.106	0.076
Fractionally-Wet Beads	Oil-Water +400 Pa	Unique	-1.931e-07	1.2934e-04	2.879e-06	0.344	-0.178	0.066	0.008
		Drainage	-1.968e-06	-0.003	0.004	-1.675	0.953	0.900	Undefined
		Imbibition	2.303e-06	-0.002	0.009	-1.567	1.210	0.469	Undefined
	Air-Oil	Unique	-6.127e-05	0.019	8.453e-04	0.498	-1.242	-1.181	0.021
		Drainage	7.748e-05	-0.031	-0.006	2.093	-1.720	3.345	Undefined
		Imbibition	2.270e-05	-0.005	-0.009	2.641	-4.153	0.487	Undefined